

K-mouflage cosmology: formation of large-scale structures

Philippe Brax, Patrick Valageas

▶ **To cite this version:**

Philippe Brax, Patrick Valageas. K-mouflage cosmology: formation of large-scale structures. Physical Review D, 2014, 90, pp.023508. 10.1103/PhysRevD.90.023508 . cea-00982373

HAL Id: cea-00982373
https://cea.hal.science/cea-00982373

Submitted on 24 Feb 2021

HAL is a multi-disciplinary open access archive for the deposit and dissemination of scientific research documents, whether they are published or not. The documents may come from teaching and research institutions in France or abroad, or from public or private research centers.

L'archive ouverte pluridisciplinaire **HAL**, est destinée au dépôt et à la diffusion de documents scientifiques de niveau recherche, publiés ou non, émanant des établissements d'enseignement et de recherche français ou étrangers, des laboratoires publics ou privés.

K-mouflage Cosmology: Formation of Large-Scale Structures

Philippe Brax and Patrick Valageas
Institut de Physique Théorique,
CEA, IPhT, F-91191 Gif-sur-Yvette, Cédex, France
CNRS, URA 2306, F-91191 Gif-sur-Yvette, Cédex, France
(Dated: September 22, 2018)

We study structure formation in K-mouflage cosmology whose main feature is the absence of screening effect on quasilinear scales. We show that the growth of structure at the linear level is affected by both a new time dependent Newton constant and a friction term which depend on the background evolution. These combine with the modified background evolution to change the growth rate by up to ten percent since $z \sim 2$. At the one loop level, we find that the nonlinearities of the K-mouflage models are mostly due to the matter dynamics and that the scalar perturbations can be treated at tree level. We also study the spherical collapse in K-mouflage models and show that the critical density contrast deviates from its Λ-CDM value and that, as a result, the halo mass function is modified for large masses by an order one factor. Finally we consider the deviation of the matter spectrum from Λ-CDM on nonlinear scales where a halo model is utilized. We find that the discrepancy peaks around 1 $h\mathrm{Mpc}^{-1}$ with a relative difference which can reach fifty percent. Importantly, these features are still true at larger redshifts, contrary to models of the chameleon-$f(R)$ and Galileon types.

PACS numbers: 98.80.-k

arXiv:1403.5424v2 [astro-ph.CO] 30 Nov 2014

I. INTRODUCTION

Scalar fields could be crucial in explaining the recent acceleration of the expansion of the Universe [1]. They could also modify gravity as described by General Relativity (GR) [2]. Such scalar fields with low masses could affect the growth of structures on very large scales in the Universe. On the other hand, in the Solar System or the laboratory, modifications of General Relativity are tightly constrained [3]. The compatibility between the two behaviors on large and small scales can be ascertained in screened modified gravity where environmental effects take place in the presence of matter. In this paper, we study the formation of structure in K-mouflage models [4, 5]. The background cosmology has been analyzed in a companion paper [6].

The K-mouflage mechanism is present in scalar field theories with noncanonical kinetic terms. It is effective in regions of space where the gravitational acceleration is larger than a critical value [7]. On large scales where matter is less dense, deviations from GR can be significant and affect the growth of structure. In particular, K-mouflage models do not converge towards GR in the large distance regime. As a result, K-mouflage models behave like a linear theory with a time dependent Newton constant up to quasilinear scales.

We study the perturbative regime of K-mouflage models before analyzing the nonlinear regime. Linear perturbation theory differs from Λ-CDM on large scales and is therefore amenable to clean comparisons with the measurements of the growth factor as forecast by the EUCLID mission [8]. It turns out that the linear regime in the scalar sector gives a good description of the growth structure up to quasilinear scales owing to the relative irrelevance of nonlinear corrections in the scalar sector. In the nonlinear regime, we use the spherical collapse to deduce the halo mass function and the deviation of the power spectrum from Λ-CDM. As expected the halo mass function is significantly affected for large masses while the power spectrum can see large deviations on nonlinear scales of order 1 Mpc. This is a feature of $f(R)$ models too [9] which could be disentangled here inasmuch as it persists even for moderate redshifts in the K-mouflage case. In fact, the redshift dependence of the deviations from GR is also very different in models with the Vainshtein property such as Galileons [10, 11], with fewer deviations at moderate redshifts than in the K-mouflage models. Hence we can expect that the three screening mechanisms could be disentangled by both analyzing the large-scale features, as chameleonlike models converge to GR contrary to K-mouflage and Vainshtein models, and the time evolution of their deviations from GR, as K-mouflage models show persistent ones up to $z = 2$.

In section II, we introduce K-mouflage models, screening and the background cosmology. In section III, we analyze the perturbative regime of K-mouflage theories. In section IV, we focus on large scales and the ISW effect. In section V, we study the spherical collapse and apply these results to a halo model which allows us to tackle the cosmology of nonlinear scales. Finally in section VI, we calculate the power spectrum including nonlinearities as defined by a halo model. In section VII, we compare our results with chameleonlike models and Galileons. We conclude in section VIII. Two appendices present the perturbation theory of K-mouflage models and a comparison of the power spectrum in K-mouflage models with the one where the only modification from Λ-CDM is due to the K-mouflage background cosmology.

II. K-MOUFLAGE

We recall in this section the definition of the K-mouflage models that we consider and the evolution of the cosmological background.

A. Definition of the model

We consider scalar field models where the action in the Einstein frame has the form

$$S = \int \mathrm{d}^4x\,\sqrt{-g}\left[\frac{M_{\rm Pl}^2}{2}R+\mathcal{L}_\varphi(\varphi)\right] + \int \mathrm{d}^4x\,\sqrt{-\tilde{g}}\,\mathcal{L}_{\rm m}(\psi_{\rm m}^{(i)},\tilde{g}_{\mu\nu}), \quad (1)$$

where g is the determinant of the metric tensor $g_{\mu\nu}$, and $\psi_{\rm m}^{(i)}$ are various matter fields. The scalar field φ is explicitly coupled to matter via the Jordan-frame metric $\tilde{g}_{\mu\nu}$, which is given by the conformal rescaling

$$\tilde{g}_{\mu\nu} = A^2(\varphi)\,g_{\mu\nu}, \quad (2)$$

and $\tilde{g}$ is its determinant. We have already considered various canonical scalar field models in previous works [9, 12], with $\mathcal{L}_\varphi = -(\partial\varphi)^2/2 - V(\varphi)$. In this paper, we consider models with a nonstandard kinetic term

$$\mathcal{L}_\varphi(\varphi) = \mathcal{M}^4\,K(\chi) \quad \text{with} \quad \chi = -\frac{1}{2\mathcal{M}^4}\,\partial^\mu\varphi\,\partial_\mu\varphi. \quad (3)$$

[We use the signature $(-,+,+,+)$ for the metric.] The constant $\mathcal{M}^4$ is an energy scale of the order of the current energy density to retrieve the late-time accelerated expansion of the Universe. The canonical behavior with a cosmological constant, $\rho_\Lambda = \mathcal{M}^4$ [see Eq.(22) below], is obtained in the weak-χ limit when:

$$\chi \to 0: \quad K(\chi) \simeq -1 + \chi + ..., \quad (4)$$

where the dots stand for higher-order terms. We have chosen the minus sign of the constant -1 at $\chi = 0$ using $\rho_\Lambda = -\mathcal{M}^4K(0) > 0$ (for the models where the late-time behavior corresponds to $\chi \to 0$).

The dynamics are determined by the Klein-Gordon equation which reads now as

$$\frac{1}{\sqrt{-g}}\partial_\mu\left[\sqrt{-g}\,\partial^\mu\varphi\,K'\right] - \frac{\mathrm{d}\ln A}{\mathrm{d}\varphi}\,\rho_E = 0, \quad (5)$$

where $\rho_E = -g^{\mu\nu}T_{\mu\nu}$ is the Einstein-frame matter density, and we note with a prime $K' = \mathrm{d}K/\mathrm{d}\chi$.

B. Screening

The suppression of the scalar field effect in dense environments due to K-mouflage is significant when the gradient of the scalar field satisfies

$$|\nabla\varphi| \gtrsim \mathcal{M}^2 \quad (6)$$

implying that a necessary condition on the Newtonian potential $\Psi_{\rm N}$ for screening in K-mouflage models is

$$|\nabla\Psi_{\rm N}| \gtrsim \frac{\mathcal{M}^2}{2\beta M_{\rm Pl}} \quad (7)$$

where the coupling to matter $\beta = M_{\rm Pl}\frac{\mathrm{d}\ln A}{\mathrm{d}\varphi}$ is a slowly varying function of φ. For the Newtonian potential around a dense object of mass m, screening occurs inside the K-mouflage radius

$$R_K = \left(\frac{\beta m}{4\pi M_{\rm Pl}\mathcal{M}^2}\right)^{1/2}. \quad (8)$$

For quasilinear scales in cosmology, screening appears when the wave number $k = 1/x$ characterizing a given structure satisfies

$$k \lesssim 3\Omega_{\rm m0}A(\varphi_0)\beta(\varphi_0)\frac{H_0^2M_{\rm Pl}}{\mathcal{M}^2}\delta, \quad (9)$$

where $\delta = (\rho-\bar{\rho})/\bar{\rho}$ is the matter density contrast. When $\mathcal{M}^4 \sim 3\Omega_{\Lambda0}M_{\rm Pl}^2H_0^2$ to reproduce the late-time cosmological constant, we find that

$$\frac{k}{H_0} \lesssim \sqrt{\frac{3}{\Omega_{\Lambda0}}}\Omega_{\rm m0}A(\varphi_0)\beta(\varphi_0)\delta \quad (10)$$

which is associated to superhorizon scales. As a result, all quasilinear objects in the Universe are unscreened in K-mouflage models.

Therefore, we expect that linear scales are maximally affected in K-mouflage models. In particular the integrated Sachs-Wolfe effect becomes relevant, where we have the approximation

$$\frac{\Delta T_{\rm ISW}}{T_{\rm CMB}} \approx \frac{2}{c^2}\int_{\tau_{\rm LS}}^{\tau_0}\mathrm{d}\tau\;\partial_\tau\Psi_{\rm N} \quad (11)$$

between the last scattering and now. Here $\tau = \int \mathrm{d}t/a$ is the conformal time and we have approximated the visibility function by unity after the last scattering and zero at earlier times. Using the Poisson equation and defining by D_+ the matter density growing mode of linear perturbation theory, we find that on the largest scales the Integrated Sachs-Wolfe effect behaves like

$$\frac{\Delta T_{\rm ISW}}{T_{\rm CMB}} \approx \frac{2}{c^2}\left[\Psi_{\rm N}(\tau_0) - \Psi_{\rm N}(\tau_{\rm LS})\right] \propto \left(\bar{A}_0D_{+0} - \frac{\bar{A}_{\rm LS}D_{+\rm LS}}{a_{\rm LS}}\right). \quad (12)$$

As a result, in K-mouflage models both the growth of structure (through D_+) and the background cosmology (through the variation of the function $A(\bar{\varphi})$ as a function of the background field $\bar{\varphi}$) can lead to a significant change in the ISW effect from Λ-CDM. We will analyze this effect in more details in Sec. IV.

C. Specific models

We use the same three models as in the companion paper [6] where we study the background evolution for

$$\text{“no-}\chi_*\text{”}\ K' \geq 1\ :\quad K(\chi) = -1 + \chi + K_0\,\chi^m,\quad K_0 > 0,\ \ m \geq 2, \tag{13}$$

$$\text{“with-}\chi_*\text{”}\ K' \leq 0\ :\quad K(\chi) = -1 + \chi + K_0\,\chi^m,\quad K_0 < 0,\ \ m \geq 2, \tag{14}$$

and

$$\text{“with-}\chi_*\text{”}\ K' \geq 0\ :\quad K(\chi) = -1 + \chi - \chi^2 + \chi^3/4. \tag{15}$$

The first model (13) corresponds to scenarios where K' never comes across a zero (“no-χ_*”) during the background cosmological evolution and remains positive. The second and third models correspond to scenarios where K' comes across a zero, $\chi_* > 0$, at late times (in fact, at infinite time), from below [Eq.(14)] or from above [Eq.(15)], as χ rolls down from $+\infty$.

More generally, the first two terms in Eq.(13), $(-1+\chi)$, represent the first-order expansion in χ of a generic function $K(\chi)$, as in Eq.(4), so that we recover a canonical scalar field with a cosmological constant for small time and spatial gradients. The third term $K_0\,\chi^m$ represents the large-χ behavior of the function $K(\chi)$, or more precisely the relevant exponent at the time of interest.

As shown in the companion paper [6], the models (14) actually show ghost instabilities. In particular, vacuum decay leads to a large production of photons and observational constraints on the diffuse gamma ray background yield an upper bound on the cutoff scale Λ of the theory. This gives $\Lambda \leq 1$ keV for $m = 2$ and $\Lambda \leq 4$ eV for $m = 3$, hence these models are not very realistic. Nevertheless, we include them in our study for illustration.

For the coupling function $A(\varphi)$, we again consider the simple power laws,

$$n \in \mathbb{N},\ \ n \geq 1\ :\quad A(\varphi) = \left(1 + \frac{\beta\varphi}{n M_{\rm Pl}}\right)^n, \tag{16}$$

which include the linear case $n = 1$, and the exponential limit for $n \to +\infty$,

$$A(\varphi) = e^{\beta\varphi/M_{\rm Pl}}. \tag{17}$$

Without loss of generality, we normalized the field φ (by the appropriate additive constant) so that $A(0) = 1$.

The action (1) is invariant with respect to the transformation $(\varphi, \beta) \to (-\varphi, -\beta)$; therefore, we can choose $\beta > 0$. Thus, in addition to the usual cosmological parameters, our system is defined by the five parameters

$$\{\beta, n; K_0, m; \mathcal{M}^4\}\ \text{ with }\ \beta > 0,\ \mathcal{M}^4 > 0,\ n \geq 1,\ m \geq 2, \tag{18}$$

except for the model (15) where there are no parameters $\{K_0, m\}$ as the kinetic function is fixed. The scale $\mathcal{M}$ is not an independent parameter. For a given value of the set $\{\beta, n; K_0, m\}$ and of H_0, it is fixed by the value of $\Omega_{\rm m0}$ today. Thus, as in the companion paper [6], in the numerical computations below, we choose the same set of cosmological parameters today, given by the Planck results [13]. Then, for any set $\{\beta, n; K_0, m\}$, we tune $\mathcal{M}$ to obtain the observed dark energy density today. As noticed above, this means that $\mathcal{M}^4 \sim \bar\rho_{\rm de0}$.

D. Cosmological background

We focus on the matter era and we only consider non-relativistic pressureless matter and the scalar field φ. Then, as shown in the companion paper [6], the Friedmann equations read

$$3M_{\rm Pl}^2 H^2 \ = \ \bar\rho + \bar\rho_\varphi^{\rm eff}, \tag{19}$$

$$-2M_{\rm Pl}^2 \dot H \ = \ \bar\rho + \bar\rho_\varphi^{\rm eff} + \bar p_\varphi, \tag{20}$$

where ρ is the conserved matter density, which is defined in terms of the Einstein-frame matter density ρ_E by

$$\rho = A^{-1}\rho_E, \quad \text{and} \quad \dot{\bar\rho} = -3H\,\bar\rho \ \text{ hence } \ \bar\rho = \frac{\bar\rho_0}{a^3}, \tag{21}$$

ρ_φ and p_φ, are the scalar field energy density and pressure (in the Einstein frame),

$$\bar\rho_\varphi = -\mathcal{M}^4\bar K + \dot{\bar\varphi}^2\,\bar K', \quad \bar p_\varphi = \mathcal{M}^4\bar K, \tag{22}$$

and $\rho_\varphi^{\rm eff}$ is the effective scalar field density, defined by

$$\rho_\varphi^{\rm eff} = \rho_\varphi + [A(\varphi) - 1]\rho, \tag{23}$$

which satisfies the standard conservation equation (the pressure p_φ is not modified)

$$\dot{\bar\rho}_\varphi^{\rm eff} = -3H(\bar\rho_\varphi^{\rm eff} + \bar p_\varphi). \tag{24}$$

Here and in the following, the overbar denotes background uniform quantities.

The Klein-Gordon equation (5) reads as

$$\partial_t\left(a^3\dot{\bar\varphi}\bar K'\right) = -\frac{{\rm d}\bar A}{{\rm d}\bar\varphi}\,\bar\rho\,a^3, \tag{25}$$

and the relevant cosmological solution is the solution of the integrated form

$$t \geq 0\ :\quad a^3\dot{\bar\varphi}\bar K' = -\int_0^t {\rm d}t'\ \bar\rho_0 \frac{{\rm d}\bar A}{{\rm d}\bar\varphi}(t'), \tag{26}$$

with the boundary condition $\bar\varphi \to 0$ at $t \to 0$. This gives the early-time power law behaviors

$$t \to 0\ :\ |\bar\varphi| \sim t^{2(m-1)/(2m-1)},\ \ |\dot{\bar\varphi}| \sim t^{-1/(2m-1)},\quad \bar\rho_\varphi^{\rm eff} \sim \bar\rho_\varphi \sim \bar p_\varphi \sim t^{-2m/(2m-1)}, \tag{27}$$

and the signs of $\bar\varphi$ and $\dot{\bar\varphi}$ are opposite to the sign of K_0,

$$t \to 0\ :\quad K_0\dot{\bar\varphi} < 0,\ \ K_0\bar\varphi < 0. \tag{28}$$

The solution (26) is an attractor tracker solution. At early times, we recover the matter era, with $\bar{\rho}_\varphi^{\rm eff} \ll \bar{\rho}$, and at late times we recover a cosmological-constant behavior, with $\bar{\rho}_{\rm de} = \mathcal{M}^4$ for the models (13) and $\bar{\rho}_{\rm de} = -\mathcal{M}^4 K(\chi_*)$ for the models (14) and (15). More precisely, for $t \to \infty$, far in the dark energy era, we obtain the behaviors

$$\text{“}K' \geq 1\text{”}: \quad a(t) \sim e^{\mathcal{M}^2 t/(\sqrt{3}M_{\rm Pl})}, \quad \bar{\varphi} \to \text{constant} < 0, \tag{29}$$

$$\text{“}K' \leq 0\text{”}: \quad a(t) \sim e^{\sqrt{-K_*/3}\mathcal{M}^2 t/M_{\rm Pl}}, \quad \bar{\varphi} \simeq \sqrt{2\chi_* \mathcal{M}^4}\, t, \tag{30}$$

and

$$\text{“}K' \geq 0\text{”}: \quad a(t) \sim e^{\sqrt{-K_*/3}\mathcal{M}^2 t/M_{\rm Pl}}, \quad \bar{\varphi} \simeq -\sqrt{2\chi_* \mathcal{M}^4}\, t, \tag{31}$$

for the models (13), (14), and (15).

In addition, from Eq.(26) and the fact that $\varphi/M_{\rm Pl}$ has not grown much beyond unity until the current time t_0 (because of the BBN constraint, see the companion paper), we have

$$0 \leq t \leq t_0: \quad \left|\frac{\beta\bar{\varphi}}{M_{\rm Pl}}\right| \lesssim 1 \quad \text{and} \quad \frac{\beta\bar{\varphi}}{M_{\rm Pl}} \sim -\frac{\beta^2}{\bar{K}'}. \tag{32}$$

This sets a condition on the parameters of the model. In particular, β is typically less than unity, except for models (13) with a large value of K_0 that implies that $\bar{K}'$ has remained large until today.

III. FORMATION OF LARGE-SCALE STRUCTURES

A. Equations of motion

To derive the continuity and Euler equations that govern the matter dynamics on large scales, it is convenient to work in the Einstein frame, where the energy-momentum tensor obeys

$$D_\mu T^{\mu\nu}_{\rm (m)} = -\rho_E\, \partial^\nu \ln A. \tag{33}$$

[This follows from the conservation of the total energy-momentum tensor $T^{\mu\nu}_{\rm (m)} + T^{\mu\nu}_{(\varphi)}$ of the sum of matter and scalar field components, using the Klein-Gordon equation (5) to simplify the part $D_\mu T^{\mu\nu}_{(\varphi)}$, which gives rise to the right-hand side in Eq.(33).] Then, considering perturbations in the conformal Newtonian gauge,

$$ds^2 = a^2[-(1+2\Psi_{\rm N})d\tau^2 + (1-2\Psi_{\rm N})d\mathbf{x}^2], \tag{34}$$

where $\Psi_{\rm N}$ is Newton's gravitational potential and $\tau = \int dt/a$, Eq.(33) leads to

$$\frac{\partial \rho_E}{\partial \tau} + \nabla\cdot(\rho_E \mathbf{v}) + 3\mathcal{H}\rho_E = \rho_E \frac{\partial \ln A}{\partial \tau}, \tag{35}$$

and

$$\frac{\partial \mathbf{v}}{\partial \tau} + (\mathbf{v}\cdot\nabla)\mathbf{v} + \left(\mathcal{H} + \frac{\partial \ln A}{\partial \tau}\right)\mathbf{v} = -\nabla\left(\Psi_{\rm N} + \ln A\right), \tag{36}$$

where $\mathcal{H} = (da/d\tau)/a = aH$ is the conformal expansion rate and $\mathbf{v} = d\mathbf{x}/d\tau = a\dot{\mathbf{x}}$ is the peculiar velocity. Here and in the following, we work in the nonrelativistic ($v \ll c$) and weak field ($\Psi_{\rm N} \ll c^2$) limit. The continuity equation (35) is obtained by contracting Eq.(33) with u_ν or from its $\nu = 0$ component. The Euler equation (36) is obtained from the spatial $\nu = i$ components of Eq.(33), using Eq.(35) to simplify some terms. In these calculations, as detailed in App. A, we encounter terms of the form $\mathbf{v}\nabla \ln A$, which are of order $(v^2)' \sim \nabla v^3 \sim v\nabla\Psi_{\rm N}$ as seen from the Euler equation (36). Therefore, they are negligible in the nonrelativistic and weak field limit and must be dropped (as other terms such as ∇v^3 or $v\nabla\Psi_{\rm N}$). We omit them in Eqs.(35)-(36) and in the following. In terms of the density $\rho = A^{-1}\rho_E$ introduced in Eq.(21), the continuity equation (35) reads, as in the usual Λ-CDM case, as

$$\frac{\partial \rho}{\partial \tau} + \nabla\cdot(\rho\mathbf{v}) + 3\mathcal{H}\rho = 0, \tag{37}$$

[where we used again the fact that $\mathbf{v}\nabla \ln A$ is a higher-order correction $\sim (v^2)'$]. Thus, the density ρ is still conserved by the velocity flow, including peculiar velocities, and it corresponds to the physical matter density

Next, from the Einstein equations we obtain the Poisson equation,

$$\frac{1}{a^2}\nabla^2\Psi_{\rm N} = 4\pi\mathcal{G}(\delta\rho_E + \delta\rho_\varphi) = 4\pi\mathcal{G}(\delta\rho + \delta\rho_\varphi^{\rm eff}), \tag{38}$$

where $\delta\rho_i = \rho_i - \bar{\rho}_i$ are the density fluctuations. The scalar field density ρ_φ is still given as in Eq.(22) by

$$\rho_\varphi = -\mathcal{M}^4 K + \left(\frac{\partial\varphi}{\partial t}\right)^2 K', \tag{39}$$

and the effective scalar field density $\rho_\varphi^{\rm eff}$ by Eq.(23).

The dynamics of the scalar field are given by the Klein-Gordon equation (5), which reads as

$$\frac{1}{a^3}\frac{\partial}{\partial t}\left(a^3 \frac{\partial\varphi}{\partial t}\, K'\right) - \frac{1}{a^2}\nabla\cdot(\nabla\varphi\, K') = -\frac{dA}{d\varphi}\,\rho, \tag{40}$$

while the argument χ of the kinetic function K reads as

$$\chi = \frac{1}{2\mathcal{M}^4}\left[\left(\frac{\partial\varphi}{\partial t}\right)^2 - \frac{1}{a^2}(\nabla\varphi)^2\right], \tag{41}$$

where we again used the weak field limit $\Psi_{\rm N} \ll c^2$.

B. Small-scale (subhorizon) limit for the scalar field perturbations

In contrast with most modified-gravity models, such as chameleon scenarios [9], we cannot use the quasistatic approximation in its usual form. In such models, the scalar

field Lagrangian $\mathcal{L}_\varphi$ also contains a potential $V(\varphi)$ and the Klein-Gordon equation (40) contains an additional term, $-\mathrm{d}V/\mathrm{d}\varphi$, on the right-hand side. Then, the quasistatic approximation assumes that the background field $\bar\varphi$ follows the minimum $\bar\varphi_*(t)$ of the effective potential $V_{\rm eff}(\bar\varphi) = V(\bar\varphi)+\bar\rho(t)A(\bar\varphi)$. In the same spirit, the Klein-Gordon equation of the inhomogeneous field $\varphi = \bar\varphi + \delta\varphi$ is approximated as $a^{-2}\nabla\cdot(\nabla\varphi K') = \mathrm{d}V/\mathrm{d}\varphi + \rho\,\mathrm{d}A/\mathrm{d}\varphi$. This quasistatic approximation is valid provided $mct \gg 1$, where $m^2c^2 = \partial^2 V_{\rm eff}/\partial\varphi^2$, or one considers small scales $kct \gg 1$, and various functions such as the coupling function A or the potential V are smooth enough; see also the discussion in Sec.II.B.4 in [9]. These conditions are usually met by these models (e.g., because observational constraints from the Solar System imply a large m).

In the models studied in this paper, there is no potential V and the background field $\bar\varphi$ cannot be given by a quasistatic approximation, where time derivatives can be neglected. In contrast, it is governed by the evolution equation (26). Nevertheless, we can still consider a small-scale limit for the fluctuations of the scalar field. Thus, within a perturbative approach, we write the field φ and the kinetic variable χ as

$$\varphi = \bar\varphi + \delta\varphi, \quad \chi = \bar\chi + \delta\chi, \tag{42}$$

with

$$\bar\chi = \frac{\dot{\bar\varphi}^2}{2\mathcal{M}^4} \quad \text{and} \quad \delta\chi = -\frac{(\nabla\delta\varphi)^2}{2\mathcal{M}^4a^2}. \tag{43}$$

This means that we neglect time derivatives of the scalar field fluctuations, in the small-scale or subhorizon regime

$$ctk/a \gg 1. \tag{44}$$

In other words, as we expand the Klein-Gordon equation (40) in powers of $\delta\varphi$, for each order in $\delta\varphi$ we only keep the terms with the highest power of k, that is, with the highest order of spatial derivatives. Then, terms that would arise from the product $\dot{\bar\varphi}\partial\delta\varphi/\partial t$ in $\delta\chi$ will always be subdominant with respect to those that arise from the product $(\nabla\delta\varphi)^2$. Therefore, we can simplify the analysis by removing these subdominant terms from the start, by only keeping the contribution $(\nabla\delta\varphi)^2$ in Eq.(43). In this small-scale approximation, the Klein-Gordon equation (40) also simplifies as

$$\frac{1}{a^3}\frac{\partial}{\partial t}\left(a^3\dot{\bar\varphi}\bar K'\right) - \frac{1}{a^2}\nabla\cdot(\nabla\delta\varphi\,K') = -\frac{\mathrm{d}\bar A}{\mathrm{d}\bar\varphi}(\bar\rho+\delta\rho), \tag{45}$$

where $\delta\rho$ is the matter density fluctuation. Indeed, the time-derivative factor gives rise to terms of the form $k^{2n}(\delta\varphi)^{2n}$, the spatial-derivative factor to $k^{2n+2}(\delta\varphi)^{(2n+1)}$, and fluctuations of A to $(\delta\varphi)^n$, where powers of k count the order of spatial derivatives. Thus, terms with the highest power of k per $\delta\varphi$ arise from the spatial term. Therefore, we can remove subdominant terms by using the background values $\bar K'$ in the first term in Eq.(45) and $\mathrm{d}\bar A/\mathrm{d}\bar\varphi$ on the right-hand side. Subtracting the background solution (25) we obtain the small-scale Klein-Gordon equation for the fluctuations of the scalar field

$$\frac{1}{a^2}\nabla\cdot(\nabla\delta\varphi\,K') = \frac{\bar A\beta_1}{M_{\rm Pl}}\,\delta\rho. \tag{46}$$

Here we have introduced the dimensionless coefficients

$$\beta_n(t) = M_{\rm Pl}^n\,\frac{\mathrm{d}^n\ln A}{\mathrm{d}\varphi^n}(\bar\varphi). \tag{47}$$

This equation can be inverted to give the functional $\delta\varphi[\delta\rho]$ by using a perturbative approach. Thus, we write the expansion in powers of the nonlinear density fluctuation,

$$\delta\varphi = \sum_{n=1}^{\infty}\delta\varphi^{(n)} \quad \text{with} \quad \delta\varphi^{(n)} \propto (\delta\rho)^n, \tag{48}$$

which reads in Fourier space (which we denote with a tilde),

$$\begin{aligned}\delta\tilde\varphi(\mathbf{k}) \;=\; &\sum_{n=1}^{\infty}\int \mathrm{d}\mathbf{k}_1\ldots\mathrm{d}\mathbf{k}_n\;\delta_D(\mathbf{k}_1+\cdots+\mathbf{k}_n-\mathbf{k})\\ &\times h_n(\mathbf{k}_1,\ldots,\mathbf{k}_n)\,\delta\tilde\rho(\mathbf{k}_1)\ldots\delta\tilde\rho(\mathbf{k}_n).\end{aligned} \tag{49}$$

Because $\delta\chi$ is quadratic in $\delta\varphi$, the left-hand side in Eq.(46) is odd in $\delta\varphi$ while the right-hand side is odd over $\delta\rho$. Therefore, we have the symmetry $(\delta\varphi,\delta\rho)\to(-\delta\varphi,-\delta\rho)$ and all even orders in the expansion (49) vanish.

One can obtain the same results by keeping all terms in Eq.(40), including terms such as $\partial\delta\varphi/\partial t$, and looking for the leading terms in the final expressions for each order $\delta\varphi^{(n)}$. More precisely, from the scalings $k^{2n}(\delta\varphi)^{2n}$ and $k^{2n+2}(\delta\varphi)^{(2n+1)}$ of the terms that arise from the time- and space-derivatives of the Klein-Gordon equation (40), one finds $\delta\varphi^{(2n+1)}\sim k^{-2n-2}$ and $\delta\varphi^{(2n)}\sim k^{-2n-2}$. Then, the even orders are subdominant with respect to the scaling $\delta\varphi^{(n)}\sim k^{-n-1}$ satisfied by the odd orders. This agrees with the result that even orders vanish in the small-scale approximation (46).

Introducing the coefficients

$$\kappa_n(t) = \frac{\mathrm{d}^n K}{\mathrm{d}\chi^n}(\bar\chi), \quad \text{and hence} \quad \bar K' = \kappa_1, \tag{50}$$

we obtain at first order

$$\frac{\kappa_1}{a^2}\nabla^2\delta\varphi^{(1)} = \frac{\bar A\beta_1}{M_{\rm Pl}}\,\delta\rho, \quad h_1(k) = \frac{-\bar A\beta_1 a^2}{\kappa_1 M_{\rm Pl}k^2}. \tag{51}$$

As explained above, the second order vanishes, $h_2 = 0$. At third order, we obtain

$$\begin{aligned}\frac{\kappa_1}{a^2}\nabla^2\cdot\delta\varphi^{(3)} \;=\; &\frac{\kappa_2}{2\mathcal{M}^4a^4}\Big\{\left[\nabla\cdot\delta\varphi^{(1)}\right]^2\nabla^2\cdot\delta\varphi^{(1)}\\ &+2\frac{\partial\delta\varphi^{(1)}}{\partial x_i}\frac{\partial\delta\varphi^{(1)}}{\partial x_j}\frac{\partial^2\delta\varphi^{(1)}}{\partial x_i\partial x_j}\Big\},\end{aligned} \tag{52}$$

hence

$$h_3(\mathbf{k}_1,\mathbf{k}_2,\mathbf{k}_3) = \frac{\kappa_2 \bar{A}^3\beta_1^3 a^4}{2\kappa_1^4\mathcal{M}^4 M_{\rm Pl}^3} \times\frac{(\mathbf{k}_1\cdot\mathbf{k}_2)k_3^2+2(\mathbf{k}_1\cdot\mathbf{k}_3)(\mathbf{k}_2\cdot\mathbf{k}_3)}{k^2k_1^2k_2^2k_3^2}. \quad (53)$$

Thus, even though the background field $\bar{\varphi}$ follows the dynamical equation (25), the fluctuations $\delta\varphi$ are described by a quasistatic approximation as time derivatives no longer appear in Eq.(46). This is possible because in the small-scale regime (44) fluctuations have enough time to relax, on a local time scale $t_k \sim a/(ck)$ that is much shorter than the Hubble time.

We can note that the quasistatic Klein-Gordon equation (46) only defines $\delta\varphi$ up to an additive constant $\delta\varphi_0$, because it only depends on gradients of $\delta\varphi$. We set this constant to zero as we require the scalar field fluctuations to vanish when the density fluctuations vanish. For a periodic density field, we can look for a periodic solution $\delta\varphi$ (thanks to the constraint $\overline{\delta\rho}=0$). This implies that at all orders $n\geq 2$ the symmetrized kernels $h_n^s(\mathbf{k}_1,..,\mathbf{k}_n)$ vanish in the limit where $\mathbf{k}=\mathbf{k}_1+..+\mathbf{k}_n$ goes to zero while the individual wave numbers $\{\mathbf{k}_1,..,\mathbf{k}_n\}$ remain finite. [This is not obvious in Eq.(53) but one can check that the symmetrized kernel $h_3^s = 1/6\sum_{\rm perm.} h_3(\mathbf{k}_1,\mathbf{k}_2,\mathbf{k}_3)$ verifies $h_3^s(\mathbf{k}_1,\mathbf{k}_2,\mathbf{k}_3)=0$ when $\mathbf{k}_1+\mathbf{k}_2+\mathbf{k}_3=0$.]

The results (51) and (53) only apply in the small-scale limit (44). In particular, the divergences at $k_i\to 0$ are not physical as these expressions are no longer valid for wave numbers below $a/(ct)$.

C. Perturbation theory

1. Fifth force and Newtonian gravity

We have described in the previous section how the Klein-Gordon equation (40) can be solved for $\varphi[\rho]$, through the perturbative expansion (49) in the density perturbation $\delta\rho$. In a second step, this allows us to solve the dynamics of the system in a perturbative manner, where we now expand in powers of the linear density field as in the standard Λ-CDM perturbation theory. This approach is identical to the method used in other modified-gravity models with a canonical kinetic term, such as chameleon scenarios, or $f(R)$ models [9]. To recover a framework that is similar to the standard GR case, we simply need to express the Newtonian gravitational potential $\Psi_{\rm N}$ and the coupling term $\ln A$ in Eq.(36) in terms of the density field. Then, the Euler and continuity equations (36)-(37) form a closed system in the fields $(\rho,\mathbf{v})$ that we can solve in a perturbative manner. The difference with the standard GR case is that the nonlinearity is no longer quadratic but includes vertices of all orders.

Using Eq.(51), we obtain from the linearized Klein-Gordon equation

$$\delta\varphi \sim \frac{\bar{A}\beta_1 a^2}{M_{\rm Pl}\kappa_1 k^2}\,\delta\rho. \quad (54)$$

Then, from the background value (32), we obtain in the small-scale regime the relative field fluctuation

$$ctk/a\gg 1: \quad \frac{\delta\varphi}{\bar{\varphi}}\sim\frac{a^2}{c^2t^2k^2}\frac{\delta\rho}{\bar{\rho}}\ll\frac{\delta\rho}{\bar{\rho}}. \quad (55)$$

From the first property (32) we also have $\bar{A}\simeq 1$, $\beta_1\simeq\beta$, $\delta A\sim\beta\delta\varphi/M_{\rm Pl}$, and

$$ctk/a\gg 1: \quad \delta\ln A\sim\frac{\delta A}{\bar{A}}\sim\frac{\beta^2a^2}{\bar{K}'c^2t^2k^2}\frac{\delta\rho}{\bar{\rho}}\ll\frac{\delta\rho}{\bar{\rho}}. \quad (56)$$

In a similar fashion, the fluctuation $\delta\chi$ scales from Eq.(43) as

$$ctk/a\gg 1: \quad \frac{\delta\chi}{\bar{\chi}}\sim\frac{a^2}{c^2t^2k^2}\left(\frac{\delta\rho}{\bar{\rho}}\right)^2\ll\left(\frac{\delta\rho}{\bar{\rho}}\right)^2. \quad (57)$$

The Newtonian gravitational potential $\Psi_{\rm N}$ is given by the modified Poisson equation (38). From Eqs.(39) and (55)-(57), we have $\delta\rho_\varphi\ll\delta\rho$ in the small-scale regime, for moderate density fluctuations, and the Poisson equation (38) simplifies as

$$ctk/a\gg 1: \quad \frac{1}{a^2}\nabla^2\Psi_{\rm N}=4\pi\mathcal{G}\bar{A}\delta\rho. \quad (58)$$

This is similar to the usual Poisson equation, with a linear dependence on the density field fluctuations, but with a time dependent effective Newton constant $\bar{A}(t)\mathcal{G}$.

From the coefficients (47), the fifth-force gravitational potential that enters the Euler equation (36) reads as

$$\Psi_{\rm A}\equiv\ln A-\ln\bar{A}=\sum_{n=1}^{\infty}\frac{\beta_n}{M_{\rm Pl}^n n!}(\delta\varphi)^n. \quad (59)$$

Substituting the expansion (49), we obtain the expansion of $\Psi_{\rm A}$ in $\delta\rho$. Together with Eq.(58), this provides the expression of the total potential, $\Psi=\Psi_{\rm N}+\Psi_{\rm A}$, as a function of the matter density,

$$\tilde{\Psi}(\mathbf{k})=\tilde{\Psi}_{\rm N}+\tilde{\Psi}_{\rm A}=\sum_{n=1}^{\infty}\int{\rm d}\mathbf{k}_1..{\rm d}\mathbf{k}_n\,\delta_D(\mathbf{k}_1+..+\mathbf{k}_n-\mathbf{k}) \times H_n(\mathbf{k}_1,..,\mathbf{k}_n)\,\delta\tilde{\rho}(\mathbf{k}_1)..\delta\tilde{\rho}(\mathbf{k}_n). \quad (60)$$

The first-order term reads as

$$H_1(k)=\frac{-a^2\bar{A}}{2M_{\rm Pl}^2k^2}\left(1+\frac{2\beta_1^2}{\kappa_1}\right). \quad (61)$$

Thus, at linear order the fifth force amplifies the Newtonian force by a scale-independent factor, $\bar{A}(1+2\beta_1^2/\kappa_1)$. The second-order term H_2 scales as k^{-4} and as the even-order terms of the expansion (49) it is subdominant, so

that $H_2 = 0$ in the small-scale regime. The third-order term reads as

$$H_3(\mathbf{k}_1,\mathbf{k}_2,\mathbf{k}_3) = \frac{\kappa_2 \bar{A}^3 \beta_1^4 a^4}{2\kappa_1^4 \mathcal{M}^4 M_{\rm Pl}^4} \times \frac{(\mathbf{k}_1\cdot\mathbf{k}_2)k_3^2 + 2(\mathbf{k}_1\cdot\mathbf{k}_3)(\mathbf{k}_2\cdot\mathbf{k}_3)}{k^2 k_1^2 k_2^2 k_3^2}, \quad (62)$$

which scales as k^{-4}. The small-scale regime that we consider here, in the expressions (61)-(62) and $H_2 = 0$, applies to density fluctuations that are not too large. More precisely, at fixed nonlinear density contrast $\delta\rho/\overline{\rho}$, in the limit $k \to \infty$ all higher-order terms are negligible and the potential Ψ becomes linear in $\delta\rho$. Then, at a given small scale $ctk/a \gg 1$, as we let the density contrast go to infinity the higher-order terms become relevant and as noticed above odd-order terms first appear while even orders remain negligible, until we further increase $\delta\rho$. Thus, the expressions (61)-(62) and $H_2 = 0$ apply in the two regimes

$$\frac{ctk}{a} \gg 1, \quad \frac{\delta\rho}{\bar{\rho}} \ll \frac{ctk}{a} : \quad \delta\varphi \simeq \delta\varphi^{(1)}, \quad \delta\Psi_{\rm A} \simeq \delta\Psi_{\rm A}^{(1)}, \quad (63)$$

and

$$\frac{ctk}{a} \gg 1, \quad \frac{ctk}{a} \lesssim \frac{\delta\rho}{\bar{\rho}} \ll \left(\frac{ctk}{a}\right)^2 : \quad \delta\varphi^{(3)} \gtrsim \delta\varphi^{(1)}, \quad \delta\varphi^{(2)} \ll \delta\varphi^{(1)}, \quad \delta\Psi_{\rm A}^{(3)} \gtrsim \delta\Psi_{\rm A}^{(1)}, \quad \delta\Psi_{\rm A}^{(2)} \ll \delta\Psi_{\rm A}^{(1)}. \quad (64)$$

Thus, in the first regime (63), associated with the small-scale limit and moderate density fluctuations, the Klein-Gordon equation can be linearized in φ and the fifth force is actually linear in density fluctuations. It is also scale independent in the sense that it multiplies the usual Newtonian force by a scale-independent factor that only depends on time, as seen in Eq.(61). This is the regime that applies to cosmological perturbation theory, although for completeness we will include the higher-order correction $\delta\Psi_{\rm A}^{(3)}$ below. More precisely, by including the cubic term $\delta\Psi_{\rm A}^{(3)}$, we include the first correction that appears as density fluctuations get large and reach $\delta\rho/\bar{\rho} \sim ctk/a$. As density fluctuations further increase, we can no longer truncate the expansions (49) and (60), as odd terms $\delta\varphi^{(2n+1)}$ become of the same order of magnitude or larger than $\delta\varphi^{(1)}$. Nevertheless, the even-order terms remain negligible until $\delta\rho/\bar{\rho} \sim (ctk/a)^2$.

In this paper, we focus on cosmological perturbations with $\delta\rho/\bar{\rho} \lesssim 200$. This corresponds to the perturbative regime for density fluctuations and to collapsed halos down to the virial radius. Then, we are in the regime (63) where the small-scale limit and the perturbative expansions (49) and (60) apply. For studies of the Solar System (or inner regions of galaxies), we should go beyond these expansions as density fluctuations become large enough to generate large scalar field fluctuations. Then, the nonlinearities of the Klein-Gordon equation become highly relevant and give rise to the K-mouflage mechanism, which ensures a convergence back to General Relativity.

As noticed in Sec.III.B of the companion paper [6], this high-density quasistatic regime corresponds to the domain $\chi < 0$ of the kinetic function $K(\chi)$, whereas cosmological perturbations around the background only probe the domain around $\bar{\chi} > 0$. Therefore, the analysis of these two classes of phenomena can be treated in an independent fashion, especially if we allow for general nonpolynomial functions $K(\chi)$ where the behaviors at $\chi \to +\infty$ and $\chi \to -\infty$ are different (e.g., with different power law exponents). We leave the study of this nonlinear screening regime to a future paper.

2. *Closed system for density and velocity fields*

In the single-stream approximation, the formation of large-scale structures is governed by the continuity and Euler equations (37) and (36). Using Eq.(56), we can neglect the fluctuations of A in Eq.(36), and the equations of motion read as

$$\frac{\partial\delta}{\partial\tau} + \nabla\cdot[(1+\delta)\mathbf{v}] = 0, \quad (65)$$

$$\frac{\partial\mathbf{v}}{\partial\tau} + (\mathbf{v}\cdot\nabla)\mathbf{v} + \left(\mathcal{H} + \frac{{\rm d}\ln\bar{A}}{{\rm d}\tau}\right)\mathbf{v} = -\nabla\Psi, \quad (66)$$

where $\delta = \delta\rho/\bar{\rho}$ is the matter density contrast and Ψ is the total potential defined in Eq.(60). Following the formalism described in [9], we can now solve the dynamics in a perturbative approach in powers of the linear density contrast δ_L. Introducing the time variable $\eta = \ln a$ and the two-component vector ψ,

$$\psi \equiv \begin{pmatrix} \psi_1 \\ \psi_2 \end{pmatrix} \equiv \begin{pmatrix} \delta \\ -(\nabla\cdot\mathbf{v})/\dot{a} \end{pmatrix}, \quad (67)$$

Eqs.(65)-(66) read in Fourier space as

$$\frac{\partial\tilde{\psi}_1}{\partial\eta} - \tilde{\psi}_2 = \int {\rm d}\mathbf{k}_1 {\rm d}\mathbf{k}_2\, \delta_D(\mathbf{k}_1+\mathbf{k}_2-\mathbf{k})\hat{\alpha}(\mathbf{k}_1,\mathbf{k}_2) \times \tilde{\psi}_2(\mathbf{k}_1)\tilde{\psi}_1(\mathbf{k}_2), \quad (68)$$

$$\frac{\partial\tilde{\psi}_2}{\partial\eta} + \frac{k^2}{a^2H^2}\tilde{\Psi} + \left(\frac{1-3w_\varphi^{\rm eff}\Omega_\varphi^{\rm eff}}{2} + \frac{{\rm d}\ln\bar{A}}{{\rm d}\eta}\right)\tilde{\psi}_2 = \int {\rm d}\mathbf{k}_1 {\rm d}\mathbf{k}_2\, \delta_D(\mathbf{k}_1+\mathbf{k}_2-\mathbf{k})\hat{\beta}(\mathbf{k}_1,\mathbf{k}_2)\tilde{\psi}_2(\mathbf{k}_1)\tilde{\psi}_2(\mathbf{k}_2), \quad (69)$$

with

$$\hat{\alpha}(\mathbf{k}_1,\mathbf{k}_2) = \frac{(\mathbf{k}_1+\mathbf{k}_2)\cdot\mathbf{k}_1}{k_1^2}, \hat{\beta}(\mathbf{k}_1,\mathbf{k}_2) = \frac{|\mathbf{k}_1+\mathbf{k}_2|^2(\mathbf{k}_1\cdot\mathbf{k}_2)}{2k_1^2k_2^2}. \quad (70)$$

In the standard Λ-CDM cosmology, where the Newtonian gravitational potential is linear in the density field, the continuity and Euler equations (68)-(69) are quadratic. In modified gravity models, such as those studied in this paper, the potential Ψ is nonlinear and contains terms of all orders in $\delta\rho$. Therefore, we must introduce vertices of all orders and we write Eqs.(68)-(69) under the more concise form

$$\mathcal{O}(x,x')\cdot\tilde{\psi}(x') = \sum_{n=2}^{\infty} K_n^s(x;x_1,..,x_n)\cdot\tilde{\psi}(x_1)\dots\tilde{\psi}(x_n), \tag{71}$$

where we have introduced the coordinates $x=(\mathbf{k},\eta,i)$, $i=1,2$ is the discrete index of the two-component vector $\tilde{\psi}$, and repeated coordinates are integrated over. The matrix $\mathcal{O}$ reads as

$$\mathcal{O}(x,x') = \delta_D(\eta'-\eta)\,\delta_D(\mathbf{k}'-\mathbf{k}) \times \begin{pmatrix} \frac{\partial}{\partial\eta} & -1 \\ -\frac{3}{2}\Omega_{\rm m}(1+\epsilon_1) & \frac{\partial}{\partial\eta}+\frac{1-3w_\varphi^{\rm eff}\Omega_\varphi^{\rm eff}}{2}+\epsilon_2 \end{pmatrix}, \tag{72}$$

where $\epsilon_1(\eta)$ and $\epsilon_2(\eta)$ are given by

$$\epsilon_1(\eta) = \bar{A}-1+\frac{2\bar{A}\beta_1^2}{\kappa_1}, \quad \epsilon_2(\eta) = \frac{{\rm d}\ln\bar{A}}{{\rm d}\eta} = \frac{\beta_1}{M_{\rm Pl}}\frac{{\rm d}\bar{\varphi}}{{\rm d}\eta}. \tag{73}$$

These scale-independent functions of time measure the deviations of the equations of motion at the linear level from the case of a Λ-CDM or uniform dark energy scenario. The function $\epsilon_1(\eta)$ is obtained from the first-order kernel of the potential Ψ as $1+\epsilon_1 = -2M_{\rm Pl}^2a^{-2}k^2\,H_1(k,\eta)$, using Eq.(61). The vertices K_n^s are equal-time vertices of the form

$$K_n^s(x;x_1,..,x_n) = \delta_D(\eta_1-\eta)..\delta_D(\eta_n-\eta) \times \delta_D(\mathbf{k}_1+..+\mathbf{k}_n-\mathbf{k})\,\gamma^s_{i;i_1,..,i_n}(\mathbf{k}_1,..,\mathbf{k}_n;\eta). \tag{74}$$

The nonzero vertices are the usual Λ-CDM ones,

$$\gamma^s_{1;1,2}(\mathbf{k}_1,\mathbf{k}_2) = \frac{\hat{\alpha}(\mathbf{k}_2,\mathbf{k}_1)}{2}, \quad \gamma^s_{1;2,1}(\mathbf{k}_1,\mathbf{k}_2) = \frac{\hat{\alpha}(\mathbf{k}_1,\mathbf{k}_2)}{2},$$

$$\gamma^s_{2;2,2}(\mathbf{k}_1,\mathbf{k}_2) = \hat{\beta}(\mathbf{k}_1,\mathbf{k}_2), \tag{75}$$

which are of order $n=2$ and do not depend on time, and the new vertices associated with the modified gravitational potential (60),

$$n\geq 2: \quad \gamma^s_{2;1,..,1}(\mathbf{k}_1,..,\mathbf{k}_n;\eta) = -\frac{k^2\bar{\rho}^n}{a^2H^2n!} \times \sum_{\rm perm.} H_n(\mathbf{k}_1,..,\mathbf{k}_n;\eta), \tag{76}$$

where we sum over all permutations of $\{\mathbf{k}_1,..,\mathbf{k}_n\}$ to obtain symmetrized kernels γ^s. The first few vertices are given by

$$\gamma^s_{2;1,1}(\mathbf{k}_1,\mathbf{k}_2) = 0, \tag{77}$$

$$\gamma^s_{2;1,1,1}(\mathbf{k}_1,\mathbf{k}_2,\mathbf{k}_3) = -\frac{9\kappa_2\bar{A}^3\beta_1^4\Omega_{\rm m}^3M_{\rm Pl}^2H^4a^2}{2\kappa_1^4\mathcal{M}^4c^2} \times\frac{(\mathbf{k}_1\cdot\mathbf{k}_2)k_3^2+2(\mathbf{k}_1\cdot\mathbf{k}_3)(\mathbf{k}_2\cdot\mathbf{k}_3)}{k_1^2k_2^2k_3^2}+2{\rm perm.}, \tag{78}$$

where "2 perm." stands for two terms obtained by circular permutations over $\{\mathbf{k}_1,\mathbf{k}_2,\mathbf{k}_3\}$.

From the analysis in Sec. III B, we can check that at all orders the vertices decay as k^2 at low k,

$$n\geq 2, \quad k\to 0: \quad \gamma^s_{2;1,..,1}(\mathbf{k}_1,..,\mathbf{k}_n)\sim k^2, \tag{79}$$

where the limit is taken by letting the sum $\mathbf{k}=\mathbf{k}_1+..+\mathbf{k}_n$ go to zero while the individual wave numbers $\{\mathbf{k}_1,..,\mathbf{k}_n\}$ remain finite [31].

3. Linear regime

On large scales, where density fluctuations are small, we can linearize the equation of motion (71). This gives $\mathcal{O}\cdot\tilde{\psi}_L=0$, where the subscript "L" denotes the linear solutions. Then, the density contrast linear modes $D_\pm(\eta)$ are given by

$$\frac{{\rm d}^2D}{{\rm d}\eta^2}+\left(\frac{1-3w_\varphi^{\rm eff}\Omega_\varphi^{\rm eff}}{2}+\epsilon_2\right)\frac{{\rm d}D}{{\rm d}\eta}-\frac{3}{2}\Omega_{\rm m}(1+\epsilon_1)D=0. \tag{80}$$

In terms of the background quantities, we have

$$|\epsilon_1| = \left|\bar{A}-1+\frac{2\bar{A}\beta_1^2}{\kappa_1}\right| \sim \left|\frac{\beta^2}{\bar{K}'}\right|, \tag{81}$$

where we used the property (32), and

$$\epsilon_2 = \frac{\beta_1}{M_{\rm Pl}}\frac{{\rm d}\bar{\varphi}}{{\rm d}\eta} \sim -\frac{\beta^2}{\bar{K}'}. \tag{82}$$

In Eq.(81) the sign of ϵ_1 cannot be determined a priori (and it can change with time as seen in Fig. 1 below) because the terms $(\bar{A}-1)\simeq\beta\bar{\varphi}/M_{\rm Pl}$ and $2\bar{A}\beta^2/\bar{K}'$ are typically of opposite signs, see Eq.(28), and of the same order.

As we have already seen, ϵ_1 corresponds to a modification of Newton's constant, while ϵ_2 appears as a friction term in the Euler equation (66). They are both of order $\beta^2/\bar{K}'$. As found in the companion paper [6], this ratio also describes the deviation of the background from the Λ-CDM scenario. In particular, it is constrained by both the BBN upper bound on the variation of particle masses, see Eq.(32), and the requirement $t_\Lambda\lesssim t_0$ that the dark energy behaves as a cosmological constant in the recent Universe.

This common dependence on the ratio $\beta^2/\bar{K}'$ could be expected from the form of the action (1). Indeed, the coupling between the scalar field φ and matter only occurs through the function $A(\varphi)$ that relates the Einstein and Jordan metrics (2) (which appears as an effective modification of gravity from the matter point of view). A

small β means that this coupling function $A(\varphi)$ becomes independent of φ and almost equal to unity, see Eqs.(16) and (17). Then, the Jordan metric becomes identical to the Einstein metric and the matter no longer feels the scalar field, which remains at the origin.

On the other hand, a large K' means that the scalar field is sensitive to the nonlinearities of the kinetic function $K(\chi)$. This gives rise to a large prefactor for time and spatial derivatives of φ, so that the scalar field is frozen to zero, plays no significant role and General Relativity is recovered. This is also the basis of the K-mouflage mechanism. Because the sign of β is irrelevant as it can be absorbed in a change of sign of φ, as noticed in the text above Eq.(18), the combination that sets the amplitude of the coupling between matter and the scalar field is the ratio β^2/K_0, or more generally $\beta^2/\bar{K}'$, in agreement with Eqs.(81)-(82).

As described in the companion paper [6], unless $|K_0| \gg 1$, we usually have $|\bar{K}'| \simeq 1$ today, and cosmological large-scale structures are also outside of their K-mouflage radius. Hence both the background and cosmological structures feel the deviation from General Relativity. However, at early times $\dot{\bar{\varphi}}$ and $\bar{K}'$ become large, so that we recover the matter-dominated era as in the Λ-CDM scenario.

Thus, observations of the background quantities and of cosmological density fluctuations are complementary, as they should be consistent with each other. Density fluctuations may provide a more sensitive probe of the deviations from General Relativity when we consider rare objects, such as clusters of galaxies, which amplify the sensitivity to the details of the dynamics. We will consider this in Sec. V below.

Because the functions $\epsilon_i(\eta)$ do not depend on scale, the linear modes $D_\pm(\eta)$ only depend on time and not on wave number, as in the Λ-CDM cosmology. As usual, we have both a linear growing mode $D_+(\eta)$ and a linear decaying mode $D_-(\eta)$. Introducing the Wronskian of Eq.(80),

$$W(\eta) = e^{-\int_0^\eta \mathrm{d}\eta' [(1-3w_\varphi^{\rm eff}\Omega_\varphi^{\rm eff})/2+\epsilon_2]}, \tag{83}$$

the decaying mode can be written as

$$D_-(\eta) = D_+(\eta) \int_\eta^\infty \mathrm{d}\eta' \, \frac{W(\eta')}{D_+(\eta')^2}. \tag{84}$$

The growing mode $D_+(\eta)$ can be directly computed from Eq.(80). As usual, we assume that the decaying mode has had time to decrease to a negligible amplitude and we write the linear regime solution as

$$\tilde{\psi}_L(\mathbf{k},\eta) = \tilde{\delta}_{L0}(\mathbf{k}) \begin{pmatrix} D_+(\eta) \\ \frac{\mathrm{d}D_+}{\mathrm{d}\eta}(\eta) \end{pmatrix}. \tag{85}$$

We show the factors $\epsilon_1(z)$ and $\epsilon_2(z)$ in Fig. 1, for the models considered in Sec. II C. At high redshifts both ϵ_1 and ϵ_2 go to zero, as $\bar{\varphi} \to 0$ and $|\bar{K}'| \to \infty$, but it appears that the convergence to zero is faster for ϵ_1. For the models (13) with $K_0 > 0$, at late times in the cosmological constant regime, from Eq.(29) we find that ϵ_2 shows an exponential decay to zero, as $\epsilon_2 \sim e^{-\sqrt{3}\mathcal{M}^2 t/M_{\rm Pl}}$, whereas ϵ_1 goes to a finite value along with $\bar{\varphi}$ and $\bar{A}$. For the models (14) and (15), where $\bar{\varphi}$ keeps increasing linearly with time while $\bar{K}'$ goes to zero, $|\epsilon_1|$ goes to infinity at an exponential rate while ϵ_2 converges to a finite value. The coefficient ϵ_2 is positive, along with $\bar{\varphi}$, for the models (14) where $\bar{K}' \leq 0$, and negative for the models (13) and (15) where $\bar{K}' \geq 0$.

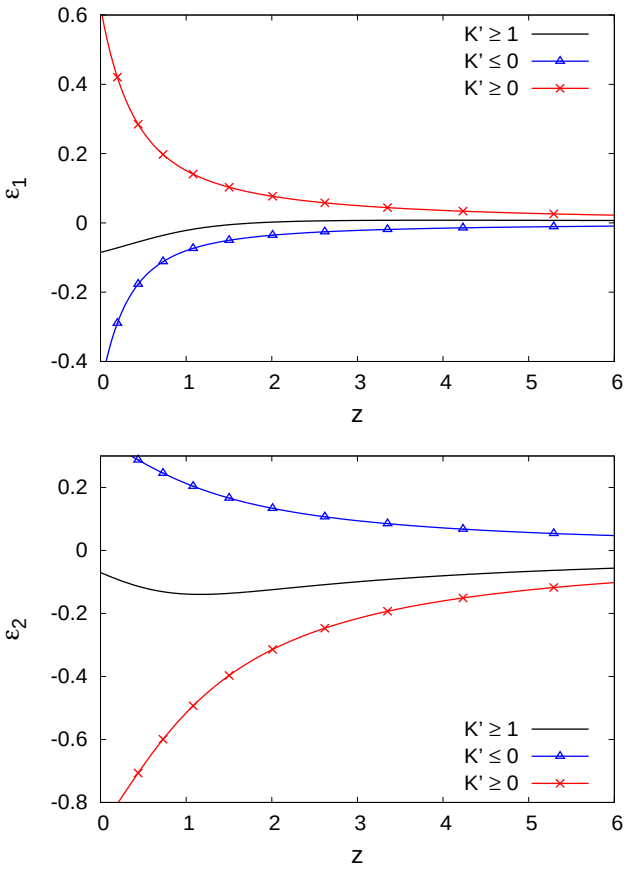


FIG. 1: *Upper panel:* factor $\epsilon_1(z)$ for the models (13) (with $K_0 = 1, m = 3$, solid line), (14) (with $K_0 = -5, m = 3$, line with triangles), and (15) (line with crosses). In all cases we use the exponential coupling function (17) with $\beta = 0.3$. *Lower panel:* factor $\epsilon_2(z)$ for the same models.

In agreement with the discussion below Eq.(82), for the models (13) the deviations from zero of the coefficients ϵ_1 and ϵ_2 are of the same order of magnitude as the deviations from Λ-CDM of the background quantities, see also Figs. 1 and 2 of the companion paper [6]. For the models (14) and (15), the deviations from Λ-CDM are somewhat amplified, as compared with the background quantities such as the Hubble expansion rate. This is because ϵ_1 diverges at late time, and ϵ_2 involves a time derivative, whereas $H(z)$ or $\Omega_{\rm m}(z)$ remain finite at late times and are constrained to be equal to the Λ-CDM reference values today.

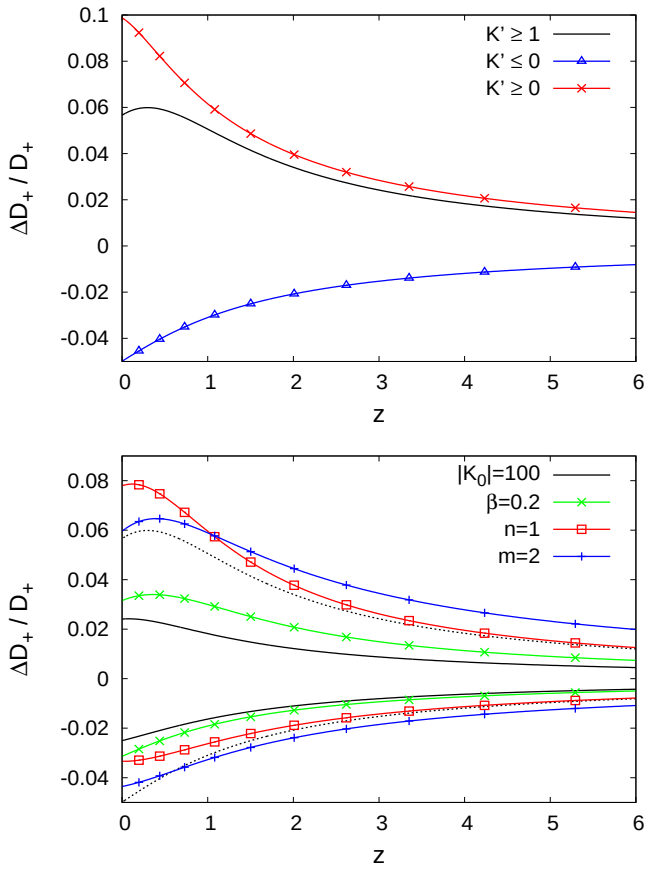


FIG. 2: Relative deviation $[D_+(z)-D_{+\Lambda\mathrm{CDM}}(z)]/D_{+\Lambda\mathrm{CDM}}(z)$ of the linear growing mode from the $\Lambda-$CDM reference. *Upper panel:* same models as in Fig. 1. *lower panel:* the upper dotted curve corresponds to the model (13) with $\{\beta = 0.3, n = \infty; K_0 = 1, m = 3\}$ (solid line in the upper panel) and the neighboring curves correspond to the same model where we modify one among these four parameters, as indicated by the legend (keeping the same sign of K_0). The lower dotted curve corresponds to the model (14) with $\{\beta = 0.3, n = \infty; K_0 = -5, m = 3\}$ (triangles in the upper panel) and the neighboring curves correspond to the same model where we again modify one among these four parameters, as indicated by the legend.

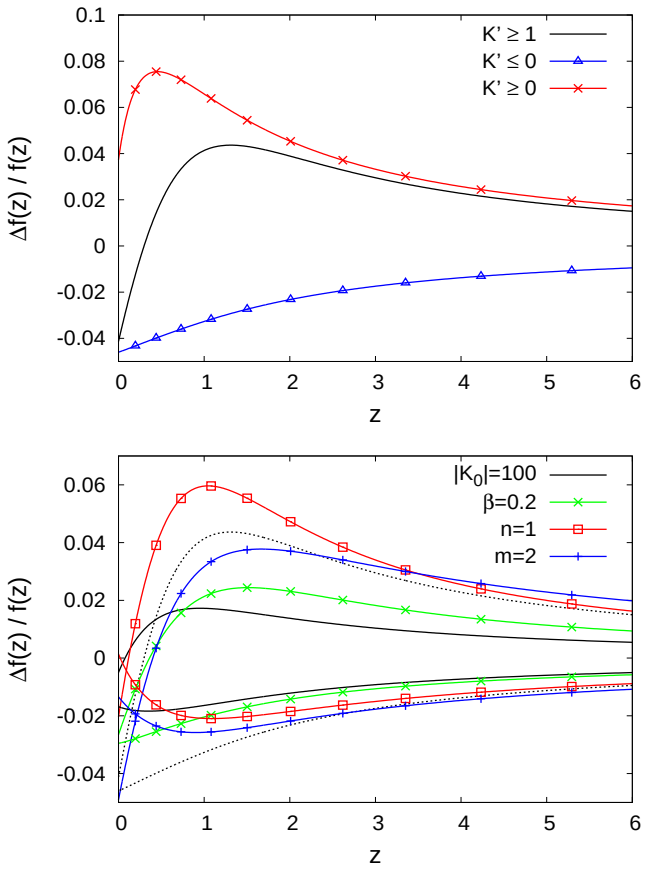


FIG. 3: Relative deviation $[f(z)-f_{\Lambda\mathrm{CDM}}(z)]/f_{\Lambda\mathrm{CDM}}(z)$ of the linear growth rate $f(z) = \mathrm{d}\ln D_+/\mathrm{d}\ln a$. *Upper panel:* same models as in the upper panel of Fig. 2. *Lower panel:* same models as in the lower panel of Fig. 2.

We show the linear growing mode $D_+(z)$ and the linear growth rate $f(z) = \mathrm{d}\ln D_+/\mathrm{d}\ln a$ in the upper panels of Figs. 2 and 3, for the same models as in Fig. 1. The relative deviations from the $\Lambda-$CDM reference are somewhat below those of the factors ϵ_i at $z = 0$ because the linear growing modes depend on the past history of these factors. As for the background expansion rate $H(z)$, the sign of $\bar{K}'$ sets the sign of the deviation from the Λ-CDM reference. Thus, the models (13) with $K_0 > 0$, and (15), which both have $\bar{K}' \geq 0$, yield a smaller $H(z)$ (when we require a common normalization today) and a larger linear growing mode $D_+(z)$, as well as a larger $f(z)$ at high redshift, while opposite deviations are obtained for the model (14) where $\bar{K}' \leq 0$. Therefore, a positive $\bar{K}'$ (resp. a negative $\bar{K}'$) yields a faster (resp. slower) growth of large-scale structures.

At early times, when the kinetic variable $\bar{\chi}$ is large and the kinetic function $K(\chi)$ is governed by the highest power law $K_0\chi^m$ in all three models (13), (14), and (15), we obtain similar behaviors for background and linear perturbation statistics, with only a change of sign along with the coefficient K_0. Thus, the high-redshift behavior is a direct probe of the sign of $\bar{K}'$ and of the large-χ power law asymptotic. At low redshift, where $\bar{\chi}$ becomes of order unity we can obtain rather different behaviors, depending on the model parameters (e.g., sign of $\bar{K}'$ and whether it goes to zero or to a nonzero value).

We consider the dependence of the linear growing modes on the model parameters in the lower panels of Figs. 2 and 3. Taking as reference the models (13) with $\{\beta = 0.3, n = \infty; K_0 = 1, m = 3\}$ and (14) with $\{\beta = 0.3, n = \infty; K_0 = -5, m = 3\}$, we show our results when we modify in turns either one of these four parameters. In agreement with the discussion below Eq.(82), the relative deviations from the $\Lambda-$CDM reference decrease for larger $|K_0|$ and smaller β^2. As for background quan-

tities, the main dependence comes from the parameters β and K_0, which set the amplitude of the coupling between the scalar field and the matter component [through the function $A(\varphi)$] and the normalization of scalar field gradients [through the function $K(\chi)$]. More precisely, the combination that sets the amplitude of the coupling between matter and the scalar field is the ratio β^2/K_0, in agreement with Eqs.(81)-(82). Changing the large-φ and large-χ behaviors of the functions $A(\varphi)$ (as n goes from $+\infty$ to 1) and $K(\chi)$ (as m goes from 3 to 2), only changes the predictions at the quantitative level and by a modest amount.

4. One-loop power spectrum

As in the standard perturbation theory, to go beyond linear order over δ_L we can look for a solution of the nonlinear equation of motion (71) as a perturbative expansion in powers of the linear density fluctuation δ_L,

$$\psi(x) = \sum_{n=1}^{\infty} \psi^{(n)}(x), \quad \text{with} \quad \psi^{(n)} \propto \delta_L^n, \tag{86}$$

and $\psi^{(1)} = \tilde{\psi}_L$. Following the general approach described in [9], to compute the higher orders $\psi^{(n)}$ by recursion from Eq.(71), we introduce the retarded Green function R_L of the linear operator $\mathcal{O}$ (also called the linear propagator or response function), which obeys:

$$\mathcal{O}(x,x') \cdot R_L(x',x'') = \delta_D(x-x''), \tag{87}$$

$$\eta_1 < \eta_2 : \quad R_L(x_1,x_2) = 0, \tag{88}$$

and reads as

$$R_L(x_1,x_2) = \frac{\Theta(\eta_1-\eta_2)\,\delta_D(\mathbf{k}_1-\mathbf{k}_2)}{D'_{+2}D_{-2} - D_{+2}D'_{-2}} \times \begin{pmatrix} D'_{+2}D_{-1} - D'_{-2}D_{+1} & D_{-2}D_{+1} - D_{+2}D_{-1} \\ D'_{+2}D'_{-1} - D'_{-2}D'_{+1} & D_{-2}D'_{+1} - D_{+2}D'_{-1} \end{pmatrix} \tag{89}$$

It involves both the linear growing and decaying modes, D_+ and D_-, and $\Theta(\eta_1-\eta_2)$ is the Heaviside function, which ensures causality. Then, from Eq.(71) we obtain at second and third order

$$\tilde{\psi}^{(2)} = R_L \cdot K_2^s \cdot \tilde{\psi}^{(1)}\tilde{\psi}^{(1)}, \tag{90}$$

$$\tilde{\psi}^{(3)} = 2R_L \cdot K_2^s \cdot \tilde{\psi}^{(2)}\tilde{\psi}^{(1)} + R_L \cdot K_3^s \cdot \tilde{\psi}^{(1)}\tilde{\psi}^{(1)}\tilde{\psi}^{(1)}. \tag{91}$$

The last term in Eq.(91) does not appear in the standard Λ-CDM case. It is due to the vertex $\gamma^s_{2;1,1,1}$ associated with the term of order $(\delta\rho)^3$ of the nonlinear modified gravitational potential Ψ. Then, the two-point correlation C_2 of the field ψ reads up to order δ_L^4 as

$$\begin{aligned} C_2(x_1,x_2) &\equiv \langle \tilde{\psi}(x_1)\tilde{\psi}(x_2)\rangle \\ &= \langle \tilde{\psi}^{(1)}\tilde{\psi}^{(1)}\rangle + \langle \tilde{\psi}^{(2)}\tilde{\psi}^{(2)}\rangle + \langle \tilde{\psi}^{(3)}\tilde{\psi}^{(1)}\rangle \\ &\quad + \langle \tilde{\psi}^{(1)}\tilde{\psi}^{(3)}\rangle + .. \end{aligned} \tag{92}$$

Defining the equal-time matter density power spectrum as

$$\langle \tilde{\delta}(\mathbf{k}_1,\eta)\tilde{\delta}(\mathbf{k}_2,\eta)\rangle = \delta_D(\mathbf{k}_1+\mathbf{k}_2)\, P(k_1,\eta), \tag{93}$$

substituting the expressions (85), (90), and (91) into Eq.(92) and using Wick's theorem, we obtain up to order P_L^2,

$$P(k) = P_{\rm tree}(k) + P_{\rm 1loop}(k). \tag{94}$$

The "tree" contribution, associated with $\langle \tilde{\psi}^{(1)}\tilde{\psi}^{(1)}\rangle$, is simply the linear power spectrum,

$$P_{\rm tree} = P_L(k), \tag{95}$$

while the "one-loop" contribution corresponds to three diagrams,

$$P_{\rm 1loop} = P_{22} + P_{31} + P_{31}^{\Psi}. \tag{96}$$

The contribution P_{22} corresponds to $\langle \tilde{\psi}^{(2)}\tilde{\psi}^{(2)}\rangle$ and P_{31} to $\langle \tilde{\psi}^{(3)}\tilde{\psi}^{(1)}\rangle + \langle \tilde{\psi}^{(1)}\tilde{\psi}^{(3)}\rangle$ using for $\tilde{\psi}^{(3)}$ the first standard term of Eq.(91). The contribution P_{31}^{Ψ} arises from the new second term of Eq.(91). More details and the diagrams associated with these one-loop contributions can be found in Ref.[9]. In particular, we obtain

$$\begin{aligned} P_{31}^{\Psi} &= 6 \int \mathrm{d}\mathbf{k}_1 \int_{-\infty}^{\eta} \mathrm{d}\eta_1\, R_{L,12}(\eta,\eta_1) C_{L,11}(k;\eta,\eta_1) \\ &\quad \times C_{L,11}(k_1;\eta_1,\eta_1)\, \gamma^s_{2;1,1,1}(\mathbf{k}_1,-\mathbf{k}_1,\mathbf{k};\eta_1), \end{aligned} \tag{97}$$

and Eq.(78) gives

$$\int \mathrm{d}\mathbf{\Omega}_{\mathbf{k}_1}\, \gamma^s_{2;1,1,1}(\mathbf{k}_1,-\mathbf{k}_1,\mathbf{k}) = \frac{30\pi\kappa_2 \bar{A}^3 \beta_1^4 \Omega_{\rm m}^3 M_{\rm Pl}^2 H^4 a^2}{\kappa_1^4 \mathcal{M}^4 c^2 k_1^2}, \tag{98}$$

where $\mathbf{\Omega}_{\mathbf{k}_1}$ is the unit vector of direction $\mathbf{k}_1$. Therefore, the angular average (98) of the vertex $\gamma^s_{2;1,1,1}$ no longer depends on the wave number k. This implies that the one-loop contribution (97) is proportional to the linear power spectrum $P_{L0}(k)$. Thus, because the modification of gravity that arises from the models studied in this paper is scale independent (in the small-scale regime $ctk/a \gg 1$ and for density fluctuations that are not too large, as explained in Secs. III B and III C 1), the vertices h_n, H_n, and γ_n do not show infrared cutoffs of the form $k^2/(m^2+k^2)$ with $m \sim 1h$/Mpc. Rather, we obtain rational functions of wave numbers that can lead to nonzero values at low k as in Eq.(98) [i.e., as compared with $f(R)$ or other scalar field models, the infrared cutoff vanishes, $m = 0$]. [The angular average Eq.(98) does not go to zero at low k, in contrast with Eq.(79), because here k_3 goes to zero along with the sum vector k.] Then, higher-order contributions generated by the modification to gravity can lead to a (small) time dependent renormalization of the linear power spectrum, in the sense that $P_{31}^{\Psi}(k) \propto P_L(k)$ at low k. From Eqs.(97)-(98) we obtain

$$P_{31}^{\Psi}(k) \sim P_L(k)\, \frac{\sigma^2_{\mathbf{s}_L} a^2}{c^2 t^2}\, \frac{\kappa_2 \beta^4}{\kappa_1^4} \ll P_L(k) \tag{99}$$

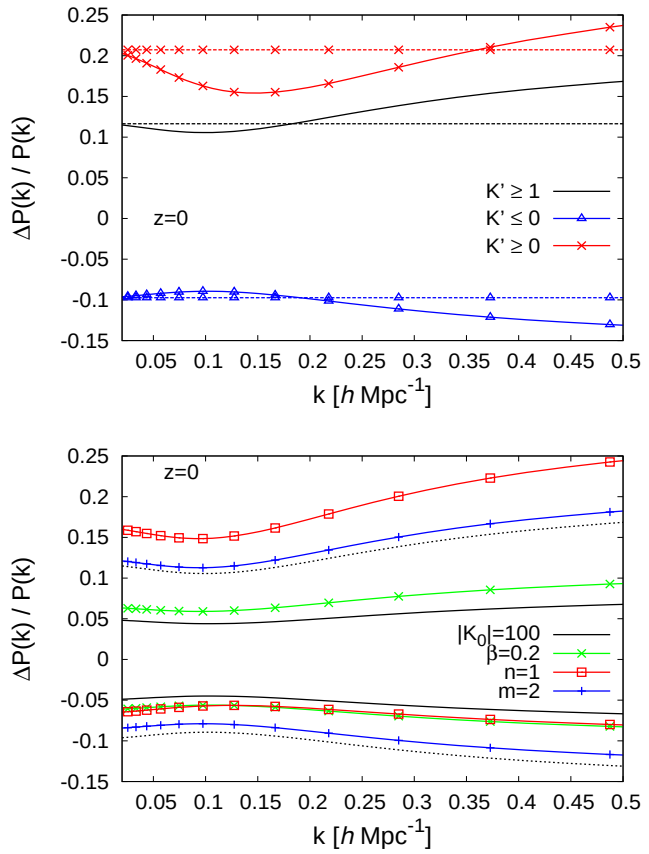


FIG. 4: Relative deviation $[P(k) - P_{\Lambda\mathrm{CDM}}(k)]/P_{\Lambda\mathrm{CDM}}(k)$ of the linear (dashed lines) and one-loop (solid lines) power spectra from the Λ-CDM reference, at redshift $z = 0$. *Upper panel:* same models as in the upper panel of Fig. 2. *Lower panel:* same models as in the lower panel of Fig. 2. We only show the one-loop power spectra (94).

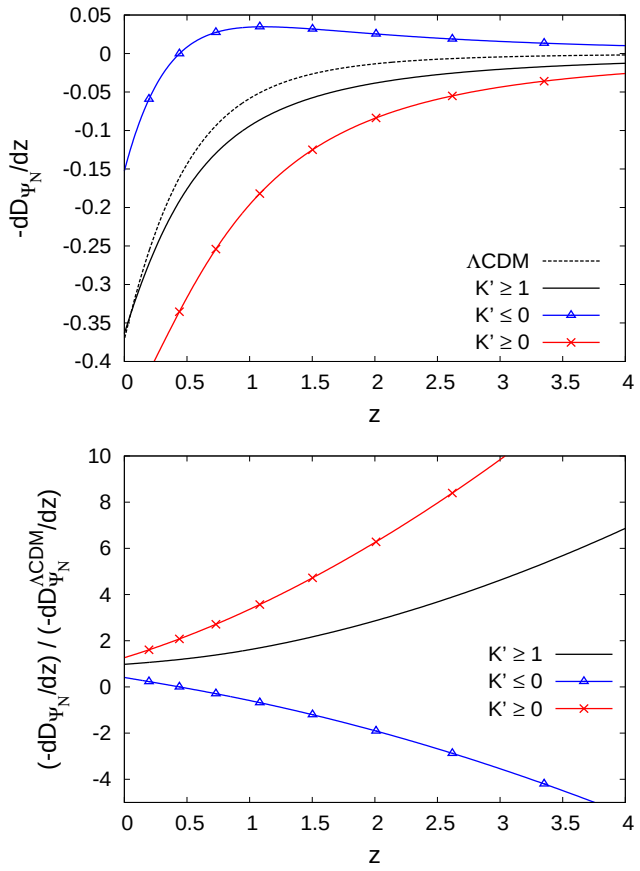


FIG. 5: *Upper panel:* the factor $(-\mathrm{d}D_{\Psi_\mathrm{N}}/\mathrm{d}z)$ of Eq.(102) for the reference Λ-CDM universe and the scenarios of Fig. 1. *Lower panel:* ratio of these factors $(-\mathrm{d}D_{\Psi_\mathrm{N}}/\mathrm{d}z)$ to the Λ-CDM reference.

where $\sigma^2_{\mathbf{s}_L} = \langle \mathbf{s}_L^2 \rangle$ is the variance of the linear displacement field [denoting $\mathbf{x}(\mathbf{q}, t) = \mathbf{q} + \mathbf{s}_L(\mathbf{q}, t)$ as the trajectory of the particle $\mathbf{q}$ in Lagrangian perturbation theory at linear order]. This shows that in the small-scale regime (63) the contribution P^Ψ_{31} is negligible, in agreement with the discussion below Eq.(63).

We show the linear and one-loop power spectra in Fig. 4. In agreement with the analysis in Sec. III C 3 and the fact that the coefficients $\epsilon_i(t)$ of Eq.(73) do not depend on scale, the relative deviation of the linear power spectrum does not depend on wave number (as long as $ctk/a \gg 1$). In agreement with Fig. 2, a positive K_0, or more generally $\bar{K}'$, leads to a speeding-up of the matter clustering, and hence a greater matter density power spectrum, while a negative K_0, or $\bar{K}'$, leads to a slower matter clustering. This remains true at one-loop order. The one-loop correction first slightly decreases the deviation from Λ-CDM, at $k \sim 0.1h\mathrm{Mpc}^{-1}$ for $z = 0$, and next amplifies the deviation at higher k when density fluctuations become mildly nonlinear (but one-loop perturbation theory does not extend beyond $0.3h$/Mpc at $z = 0$). We also checked that the one-loop contribution (97) is negligible, by comparing our results with those obtained when we set P^Ψ_{31} to zero. Thus, in agreement with the discussion below Eq.(63), the nonlinearities are not due to the Klein-Gordon equation, which can be kept at the linear level, but to the continuity and Euler equations, more precisely to the usual vertices (75), as in the standard Λ-CDM scenario.

As for previous quantities, we can see in the lower panel that deviations from the Λ-CDM predictions decrease for larger K_0 or smaller β. The detailed shape of the coupling function $A(\varphi)$ appears to have a significant impact on the power spectrum at the quantitative level, as we go from the exponential form (17) to the linear form (16).

IV. LARGE-SCALE COSMIC MICROWAVE ANISOTROPIES

A. Integrated Sachs-Wolfe effect

The Integrated Sachs-Wolfe effect (ISW) arises from the differential redshift effect that is left as photons climb in and out of time dependent gravitational potentials [14]. This generates a large-scale fluctuation, $\Delta T_{\rm ISW}$, of the cosmic microwave background (CMB), given by

$$\frac{\Delta T_{\rm ISW}}{\bar{T}_{\rm CMB}} = -\frac{2}{c^2}\int_0^\infty {\rm d}z\; e^{-\kappa(z)}\,\frac{\partial\Psi_{\rm N}}{\partial z}, \qquad (100)$$

where $\kappa(z)$ is the optical depth to redshift z. This effect can be constrained through the autocorrelation function of the temperature fluctuations of the CMB and also through the cross-correlation with the large-scale structures in the recent Universe, as galaxies and clusters are correlated with the matter density and gravitational fields [15–18]. During the matter era, on large linear scales the gravitational potential $\Psi_{\rm N}$ does not evolve with time. This means that the ISW effect is dominated by low redshifts when dark energy modifies the linear growing mode and makes $|\Psi_{\rm N}|$ decrease. This makes the ISW effect a probe of dark energy properties and of modified-gravity theories.

From the modified Poisson equation (58), we obtain in the linear regime $\nabla^2\Psi_{\rm N} = 4\pi\mathcal{G}\bar{\rho}_0\,\bar{A}\delta_L/a$, and we can write the linear mode $D_{\Psi_{\rm N}}$ of the gravitational potential as

$$D_{\Psi_{\rm N}} = \bar{A}\,\frac{D_+}{a}, \qquad (101)$$

where D_+ is the linear growing mode of the density contrast, given by Eq.(80) and displayed in Fig. 2. The ISW effect (100) involves the derivative of $D_{\Psi_{\rm N}}$ with respect to time, or redshift, and we obtain

$$-\frac{{\rm d}D_{\Psi_{\rm N}}}{{\rm d}z} = a^2\,\frac{{\rm d}D_{\Psi_{\rm N}}}{{\rm d}a} = \bar{A}D_+(\epsilon_2 + f - 1), \qquad (102)$$

where $\epsilon_2(z) = {\rm d}\ln\bar{A}/{\rm d}\ln a$ was already introduced in Eq.(73) and shown in Fig. 1, whereas $f(z) = {\rm d}\ln D_+/{\rm d}\ln a$ was shown in Fig. 3. In the standard Λ-CDM cosmology we have $\bar{A}=1$ and $\epsilon_2 = 0$.

Cross-correlations between the large-scale CMB temperature fluctuations (100) and low-redshift galaxy surveys constrain the time derivative of the gravitational potential at the redshift of the galaxy population, through the correlation $\langle\Psi_{\rm N}\delta_{\rm g}\rangle$. Therefore, we show the factor $(-{\rm d}D_{\Psi_{\rm N}}/{\rm d}z)$ as a function of redshift in the upper panel of Fig. 5.

At high z, we recover the Einstein-de Sitter cosmology and the derivative ${\rm d}D_{\Psi_{\rm N}}/{\rm d}z$ goes to zero for all models. For the modified-gravity models, we still have $\bar{A}\simeq 1$ and $f(z)$ remains close to the Λ-CDM reference, as seen in Fig. 3. Then, the main source of deviation from the Λ-CDM prediction is the new term ϵ_2 in Eq.(102). For scenarios with $\bar{K}' > 0$, we have seen in Fig. 1 that ϵ_2 is negative, like $(f-1)$. Then, $(-{\rm d}D_{\Psi_{\rm N}}/{\rm d}z)$ is negative, as in the Λ-CDM reference (i.e., linear gravitational potentials decay with time in the dark energy era). For the models (13), where ϵ_2 goes to zero at late times, the ISW factor $(-{\rm d}D_{\Psi_{\rm N}}/{\rm d}z)$ always remains close to the Λ-CDM reference, whereas for the models (15), where ϵ_2 converges to a nonzero value, the deviation remains significant at low redshift. For scenarios with $\bar{K}' < 0$, we have seen in Fig. 1 that ϵ_2 is positive and decreases slowly at high redshift. Then, the term ϵ_2 can dominate over the factor $(f-1)$ and we can see in Fig. 5 that, for the model (14) with $K_0 = -5$, $(-{\rm d}D_{\Psi_{\rm N}}/{\rm d}z)$ becomes positive at $z \gtrsim 0.4$. Therefore, in such scenarios the ISW effect changes sign at high z as the linear gravitational potential first slowly grows with time when dark energy becomes noticeable. At low redshift the term ϵ_2 is no longer dominant and $(-{\rm d}D_{\Psi_{\rm N}}/{\rm d}z)$ is negative (i.e., linear gravitational potentials decay with time) as in the standard Λ-CDM scenario. Thus, cross-correlations between the ISW effect on the CMB and large-scale structures at $z\sim 1$ would be a useful probe of such models, as the sign of the correlation itself would discriminate between the two categories $\bar{K}' > 0$ and $\bar{K}' < 0$.

The lower panel in Fig. 5 shows the ratio of $(-{\rm d}D_{\Psi_{\rm N}}/{\rm d}z)$ to the Λ-CDM reference. In agreement with the upper panel and the discussion above, this ratio remains positive for scenarios with $\bar{K}' > 0$ and becomes negative at high redshift for scenarios with $\bar{K}' < 0$. In both cases, because of the factor ϵ_2, which decays rather slowly with redshift, $(-{\rm d}D_{\Psi_{\rm N}}/{\rm d}z)$ decays more slowly than the Λ-CDM prediction at high z. This yields a ratio to the Λ-CDM reference that grows at high z. However, in practice it is difficult to probe these high-redshift behaviors, because most of the signal comes from the low-redshift range where linear gravitational potentials show a significant time dependence, as seen in the upper panel.

B. Low-ℓ CMB anisotropies

At low-ℓ multipoles, the CMB anisotropies are governed by the Sachs-Wolfe (SW) and integrated Sachs-Wolfe (ISW) effects, and the temperature fluctuation $\Delta T_{\rm CMB}/\bar{T}_{\rm CMB}$ in a direction $\vec{\gamma}$ on the sky reads as

$$\frac{\Delta T_{\rm CMB}}{\bar{T}_{\rm CMB}} \simeq \frac{1}{3c^2}\Psi_{\rm N}(\tau_{\rm LS}) + \frac{2}{c^2}\int_{\tau_{\rm LS}}^{\tau_0}{\rm d}\tau\,\frac{\partial\Psi_{\rm N}}{\partial\tau}, \qquad (103)$$

where $\tau = \int {\rm d}t/a$ is the conformal time, $\tau_{\rm LS}$ and τ_0 its value at the last-scattering surface and today. Here we have used $\Delta T/\bar{T} \simeq -2\Psi_{\rm N}/(3c^2)$ at $\tau_{\rm LS}$ and we have approximated the opacity as $\kappa = 0$ after the last-scattering surface and $\kappa = +\infty$ before. The first term in Eq.(103) is the Sachs-Wolfe effect (due to the initial temperature fluctuation and gravitational potential) and the second term is the integrated Sachs-Wolfe effect (100). Expanding as usual the temperature fluctuations on the sky in

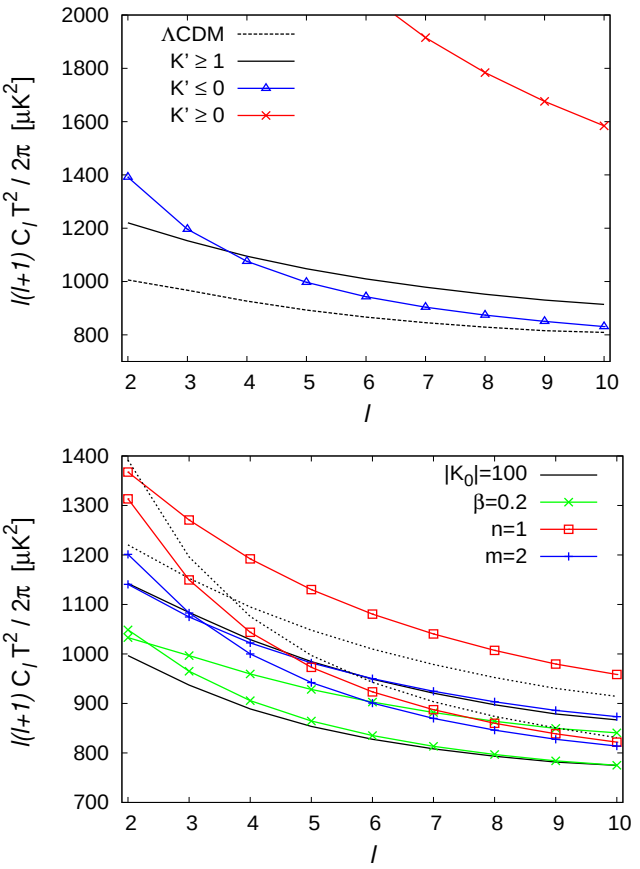


FIG. 6: CMB angular power spectrum $\ell(\ell+1)C_\ell\bar{T}^2/(2\pi)$ at low multipoles. *Upper panel:* same models as in the upper panel of Fig. 2. *Lower panel:* same models as in the lower panel of Fig. 2.

spherical harmonics, $\Delta T(\vec{\gamma})/\bar{T} = \sum_{\ell,m} a_{\ell,m} Y^\ell_m(\vec{\gamma})$, and defining the multipole power spectrum as $\langle a_{\ell,m} a^*_{\ell',m'}\rangle = \delta_{\ell,\ell'}\delta_{m,m'}C_\ell$, we obtain

$$C_\ell = (4\pi)^2 \int_0^\infty \mathrm{d}k k^2\, P_{\Psi_\mathrm{N},0}(k)\left\{\frac{D_{\Psi_\mathrm{N}}(\tau_\mathrm{LS})}{3} j_\ell[kc(\tau_0-\tau_\mathrm{LS})] + 2\int_{\tau_\mathrm{LS}}^{\tau_0}\mathrm{d}\tau \frac{\mathrm{d}D_{\Psi_\mathrm{N}}}{\mathrm{d}\tau} j_\ell[kc(\tau_0-\tau)]\right\}^2, \quad (104)$$

where we have defined the gravitational potential linear power spectrum as $\langle\tilde{\psi}_\mathrm{N}(\mathbf{k}_1,\tau_1)\tilde{\psi}_\mathrm{N}(\mathbf{k}_2,\tau_2)\rangle = \delta_D(\mathbf{k}_1+\mathbf{k}_2)\, D_{\Psi_\mathrm{N}}(\tau_1) D_{\Psi_\mathrm{N}}(\tau_2)\, c^4 P_{\Psi_\mathrm{N},0}(k_1)$, and the linear mode D_{Ψ_N} was given in Eq.(101). Because we only consider low multipoles ℓ, and hence large scales and low wave numbers k, we write the linear power spectrum as

$$P_{\Psi_\mathrm{N},0}(k) = \mathcal{N}\, k^{n_s-4}, \quad (105)$$

and the integration over k yields

$$C_\ell = \frac{2^{n_s}\pi^3\mathcal{N}\,\Gamma[\ell+\frac{n_s-1}{2}]}{c^{n_s-1}\Gamma[2-\frac{n_s}{2}]}\left\{\frac{D_{\Psi_\mathrm{N}}(\tau_\mathrm{LS})^2(\tau_0-\tau_\mathrm{LS})^{1-n_s}\Gamma[3-n_s]}{9\,\Gamma[2-\frac{n_s}{2}]\,\Gamma[\ell+\frac{5-n_s}{2}]}\right.$$
$$+4\int_{\tau_\mathrm{LS}}^{\tau_0}\mathrm{d}\tau_1\mathrm{d}\tau_2\,\frac{\mathrm{d}\,D_{\Psi_\mathrm{N}}}{\mathrm{d}\tau}(\tau_1)\frac{\mathrm{d}\,D_{\Psi_\mathrm{N}}}{\mathrm{d}\tau}(\tau_2)$$
$$\times\frac{(\tau_0-\tau_1)^\ell(\tau_0-\tau_2)^\ell\;{}_2F_1(\ell+\frac{n_s-1}{2},\ell+1;2\ell+2;y_{12})}{(2\tau_0-\tau_1-\tau_2)^{2\ell+n_s-1}\,\Gamma[\ell+\frac{3}{2}]}$$
$$+\frac{4D_{\Psi_\mathrm{N}}(\tau_\mathrm{LS})}{3}\int_{\tau_\mathrm{LS}}^{\tau_0}\mathrm{d}\tau\,\frac{\mathrm{d}\,D_{\Psi_\mathrm{N}}}{\mathrm{d}\tau}(\tau)\,\frac{(\tau_0-\tau)^\ell(\tau_0-\tau_\mathrm{LS})^\ell}{(2\tau_0-\tau-\tau_\mathrm{LS})^{2\ell+n_s-1}}$$
$$\left.\times\frac{{}_2F_1(\ell+\frac{n_s-1}{2},\ell+1;2\ell+2;y)}{\Gamma[\ell+\frac{3}{2}]}\right\}, \quad (106)$$

where the arguments of the hypergeometric functions are $y_{12} = 4(\tau_0-\tau_1)(\tau_0-\tau_2)/(2\tau_0-\tau_1-\tau_2)^2$ and $y = 4(\tau_0-\tau)(\tau_0-\tau_\mathrm{LS})/(2\tau_0-\tau-\tau_\mathrm{LS})^2$. The first term in Eq.(106) comes from the Sachs-Wolfe effect, $(\mathrm{SW})^2$, the second term from the integrated Sachs-Wolfe effect, $(\mathrm{ISW})^2$, and the third term from the cross-correlation (SW) × (ISW).

We show the CMB power spectrum on large angular scales, from Eq.(106), in Fig. 6. We compare the modified gravity-scenarios to the Λ-CDM reference in the upper panel, and we consider the sensitivity to other model parameters in the lower panel. The $(\mathrm{SW})^2$ contribution is the same in all scenarios, because we recover the Λ-CDM cosmology and the same initial conditions at early times.

In agreement with Fig. 5, for the models with $\bar{K}' > 0$ the ISW effect is greater than the Λ-CDM prediction and of opposite sign to the SW effect ($\mathrm{d}D_{\Psi_\mathrm{N}}/\mathrm{d}\tau$ is negative). It happens that the greater value of $(\mathrm{ISW})^2$ more than compensates the lower value of (SW)×(ISW) (which has a greater amplitude but is negative) and the full CMB power spectrum C_ℓ is larger than the Λ-CDM prediction.

For the models with $\bar{K}' < 0$, the ISW effect is smaller than in the Λ-CDM case and its has a different sign, because as seen in Fig. 5 the time derivative $\mathrm{d}D_{\Psi_\mathrm{N}}/\mathrm{d}\tau$ is now positive at high redshifts, $z \gtrsim 0.4$. Then, the $(\mathrm{ISW})^2$ contribution is smaller than the Λ-CDM prediction but the cross-term (SW)×(ISW) is now positive and this more than compensates the decrease of $(\mathrm{ISW})^2$, and the full CMB power spectrum C_ℓ is again larger than the Λ-CDM result.

Although low-ℓ measurements have large error bars due to the cosmic variance, the model (15) shown in the upper panel of Fig. 6 is already excluded by data (e.g., WMAP9 [19]). However, as shown in the upper and lower panels, the exact values of C_ℓ depend on the parameters of the model and low-ℓ measurements of C_ℓ cannot rule out the full class of models. In particular, it might be possible to choose parameters, or functions $K(\chi)$ and $A(\varphi)$, so that the net effect is to decrease the CMB power spectrum at the lowest ℓ, which would provide a better match to data than the Λ-CDM reference. However, we have not made a detailed search of the parameter space to find out whether such a result can be

achieved. On the other hand, the results shown in Fig. 6 suggest that "generic" models typically yield a stronger growth of the CMB power at low ℓ than for the Λ-CDM scenario.

V. SPHERICAL COLLAPSE

A. Spherical dynamics

From Eq.(66) the particle trajectories read in physical coordinates $(\mathbf{r}, t)$ as

$$\ddot{\mathbf{r}}+\frac{\mathrm{d}\ln\bar{A}}{\mathrm{d}t}\dot{\mathbf{r}}-\left(\frac{\ddot{a}}{a}+\frac{\dot{a}}{a}\frac{\mathrm{d}\ln\bar{A}}{\mathrm{d}t}\right)\mathbf{r}=-\nabla_r(\Psi_\mathrm{N}+\ln A), \quad (107)$$

where $\nabla_r=\nabla/a$ is the gradient operator in physical coordinates. To study the spherical collapse before shell crossing, it is convenient to label each shell by its Lagrangian radius q or enclosed mass M, and to introduce its normalized radius $y(t)$ by

$$y(t)=\frac{r(t)}{a(t)q} \quad \text{with} \quad q=\left(\frac{3M}{4\pi\bar{\rho}_0}\right)^{1/3}, \quad y(t=0)=1. \quad (108)$$

In particular, the matter density contrast within radius $r(t)$ reads as

$$1+\delta(<r)=y(t)^{-3}, \quad (109)$$

where $\delta=(\rho-\bar{\rho})/\bar{\rho}$ is the matter density contrast. In terms of $y(t)$, Eq.(107) also reads as

$$\frac{\mathrm{d}^2y}{\mathrm{d}\eta^2}+\left(\frac{1-3w_\varphi^\mathrm{eff}\Omega_\varphi^\mathrm{eff}}{2}+\frac{\mathrm{d}\ln\bar{A}}{\mathrm{d}\eta}\right)\frac{\mathrm{d}y}{\mathrm{d}\eta} = -\frac{3\Omega_\mathrm{m}\,y}{8\pi\mathcal{G}\bar{\rho}\,r}\frac{\partial}{\partial r}(\Psi_\mathrm{N}+\ln A), \quad (110)$$

where as in Sec. III C we use $\eta=\ln a$ as the time coordinate.

The Newtonian potential is given by the modified Poisson equation (58), which gives in spherically symmetric configurations the Newtonian force

$$F_\mathrm{N}=-\frac{\partial\Psi_\mathrm{N}}{\partial r}=-\bar{A}\frac{\mathcal{G}\delta M(<r)}{r^2}. \quad (111)$$

The Klein-Gordon equation (46) reads in spherically symmetric configurations as

$$\frac{1}{r^2}\frac{\partial}{\partial r}\left(r^2\frac{\partial\varphi}{\partial r}\bar{K}'\right)=\frac{\bar{A}\beta_1}{M_\mathrm{Pl}}\delta\rho, \quad (112)$$

hence

$$\frac{\partial\varphi}{\partial r}=\frac{\bar{A}\beta_1}{4\pi M_\mathrm{Pl}\kappa_1}\frac{\delta M(<r)}{r^2}. \quad (113)$$

In Eqs.(107)-(113) we have assumed the small-scale regime, $ctk/a\gg1$, where relative fluctuations of A are negligible as compared with relative density fluctuations, see Eq.(56). Then, the fifth force reads from Eq.(113) as

$$F_\mathrm{A}=-\frac{\partial\ln A}{\partial r}\simeq-\frac{\beta_1}{M_\mathrm{Pl}}\frac{\partial\varphi}{\partial r}=\frac{2\beta_1^2}{\kappa_1}F_\mathrm{N}. \quad (114)$$

Thus, it is proportional to the Newtonian force (111) with a time dependent prefactor. Moreover, this prefactor is again of the form $\beta^2/\bar{K}'$, as for the deviations from Λ-CDM of the background and of particle masses, see the companion paper and Eq.(32) here, and of matter clustering in the perturbative regime, see Sec. III C 2 and Eqs.(81)-(82). This is not surprising because these are different probes of the same underlying model. Then, the equation of motion (110) of the mass shell M reads as

$$\frac{\mathrm{d}^2y}{\mathrm{d}\eta^2}+\left(\frac{1-3w_\varphi^\mathrm{eff}\Omega_\varphi^\mathrm{eff}}{2}+\epsilon_2\right)\frac{\mathrm{d}y}{\mathrm{d}\eta} +\frac{\Omega_\mathrm{m}}{2}(y^{-3}-1)y(1+\epsilon_1)=0, \quad (115)$$

where the factors ϵ_1 and ϵ_2 were defined in Eq.(73). The usual Λ-CDM dynamics are recovered when the factors ϵ_i are set to zero, and the background terms $w_\varphi^\mathrm{eff}\Omega_\varphi^\mathrm{eff}$ and Ω_m follow the Λ-CDM evolution. Moreover, we can see that the nonlinear spherical dynamics (115) involve the same factors as the evolution equation (80) of the linear modes. This is made possible by the small-scale and moderate-density regime (63), which we used to derive Eq.(115). In particular, this has allowed us to write the linearized Klein-Gordon equation (112). It is clear that if higher orders in Eq.(112) had been relevant, which is the case in the regime (64) and at higher densities, they would have given rise to new factors beyond the terms ϵ_1 and ϵ_2.

Thanks to the scale independence of the modification of gravity brought by the model studied here, in the small-scale regime (63), we preserve a key property of the spherical Λ-CDM dynamics: the motions of different mass shells are decoupled before shell crossing. This greatly simplifies the analysis of the spherical collapse. This property is not satisfied by other models of modified gravity, such as $f(R)$ theories or dilaton models, where the fifth force shows an explicit scale dependence that couples the motions of different shells. This feature only applies to the regime (63), which is sufficient for our purposes as we consider density contrast $\delta\lesssim200$. If we considered higher-density regions, such as inner galaxy cores or the Solar System, there would be a departure from the expression (114). In that case, nonlinearities of the Klein-Gordon equation become important and give rise to the K-mouflage mechanism that eventually leads to a recovery of General Relativity. We do not consider this regime in this paper.

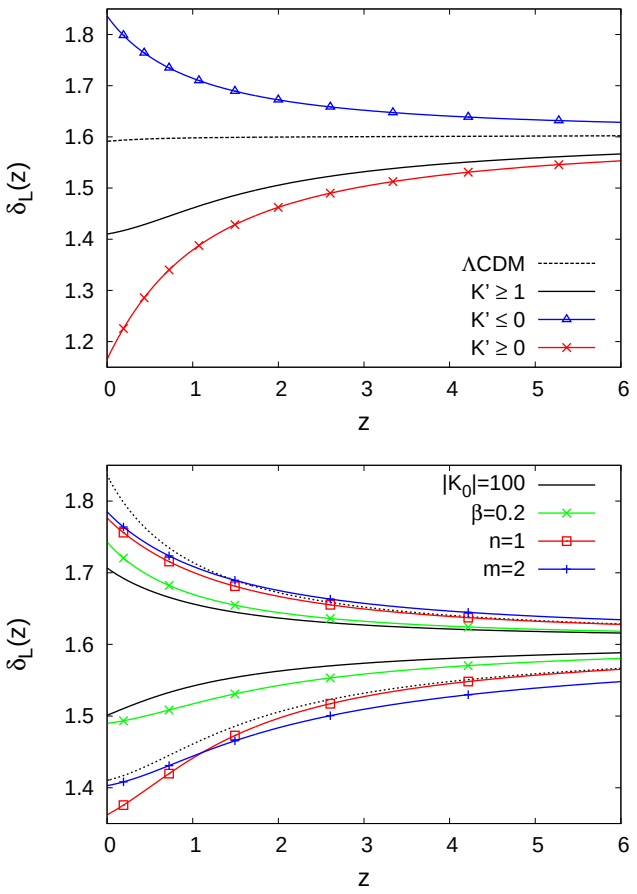


FIG. 7: Linear density contrast threshold $\delta_{L(\Lambda)}(z)$. *Upper panel:* same models as in the upper panel of Fig. 2. *Lower panel:* same models as in the lower panel of Fig. 2.

B. Linear density contrast threshold

By solving the equation of motion (115) we can numerically compute the linear density contrast threshold $\delta_L(M,z)$ that corresponds to a nonlinear density contrast of 200. (We choose a nonlinear overdensity of 200 to define virialized halos. This allows us to compare with previous works and to use the same rescaled halo mass function.) Because the modification of gravity is scale independent in the regime (63), the mass M no longer appears in the equation of motion (115). Therefore, the linear threshold $\delta_L(M,z)$ is actually independent of the halo mass M, as in the Λ-CDM scenario.

In practice, rather than the linear threshold δ_L we consider the linear threshold $\delta_{L(\Lambda)}$ associated with the initial conditions. Indeed, if we wish to estimate the impact of the modification of gravity on nonlinear matter clustering and on the halo mass function, we are not really interested in the linear density contrast today, δ_L, associated with a nonlinear density contrast $\delta = 200$, as δ_L cannot be directly observed. Rather, we are interested in the initial (or early-time) linear threshold δ_{Li}, at a high redshift z_i, which is required to produce at a later time (e..g, today) a nonlinear density contrast δ. Indeed, from δ_{Li} we can estimate from the initial Gaussian density field $\delta_{Li}(\mathbf{x})$ whether this threshold corresponds to a rare or common density fluctuation. In the usual Λ-CDM scenario, one usually "translates" both the initial linear threshold δ_{Li} and the initial density field $\delta_{Li}(\mathbf{x})$, or the root mean square density fluctuation σ_{Li}, to the present time by multiplying them by the common linear growth factor $D_+(z_0)/D_+(z_i)$. This avoids introducing the "initial" redshift z_i as initial conditions are expressed in terms of the current linear density field.

However, because we compare different cosmological scenarios, with slightly different linear growing modes but with the same high-redshift linear power spectrum, we must go back to the high redshift z_i. More precisely, to compare the efficiency of the matter clustering process between these cosmological scenarios, we wish to compare the probabilities associated with a given nonlinear threshold $\delta = 200$ today. This means that we wish to compare the initial linear thresholds δ_{Li} required in each scenario to reach the same δ today (because the initial Gaussian conditions are taken to be the same, far in the matter era). Nevertheless, to avoid introducing an explicit arbitrary high redshift z_i, and to follow the usual practice, we translate all initial thresholds δ_{Li} to the current time (or to the redshift z of interest), by multiplying all of them by the same Λ-CDM linear growth factor $D_{+\Lambda\mathrm{CDM}}(z_0)/D_{+\Lambda\mathrm{CDM}}(z_i)$. [In contrast, the "true" linear threshold δ_L in each cosmology is obtained by multiplying by its own linear growth factor $D_+(z_0)/D_+(z_i)$].

In this fashion, the comparison between the various $\delta_{L(\Lambda)}$ gives a direct hint of the various probabilities to reach $\delta = 200$ and of how far the nonlinear matter clustering is advanced between the various models, starting from the same linear power spectra at high z. In contrast, if we consider the "true" linear thresholds δ_L the comparison is biased by the fact that in different cosmologies the same δ_L actually corresponds to different initial conditions at a given high z. (Going back to the initial redshift z_i, as we implicitly do here, is also more convenient in more general modified-gravity models where the linear growing modes become scale dependent at late times.)

We show our results in Fig. 7. In agreement with the results of Sec. III C, where we have found that for models with $\bar{K}' > 0$ the scalar field accelerates the clustering of matter as it leads to greater linear growing modes and one-loop power spectra, we find that a smaller linear density contrast $\delta_{L(\Lambda)}(z)$ is required to reach the same nonlinear overdensity of 200 than in the Λ-CDM scenario. Conversely, models with $\bar{K}' < 0$ lead to a greater linear threshold $\delta_{L(\Lambda)}$. In all cases, we recover the Λ-CDM reference value at high redshift. The departure from the Λ-CDM reference grows faster at low z for the models (14) and (15) where $\bar{K}' \to 0$ at late times, in agreement with Figs. 1 and 2, and the greater amplitude of the characteristic ratio $\beta^2/\bar{K}'$.

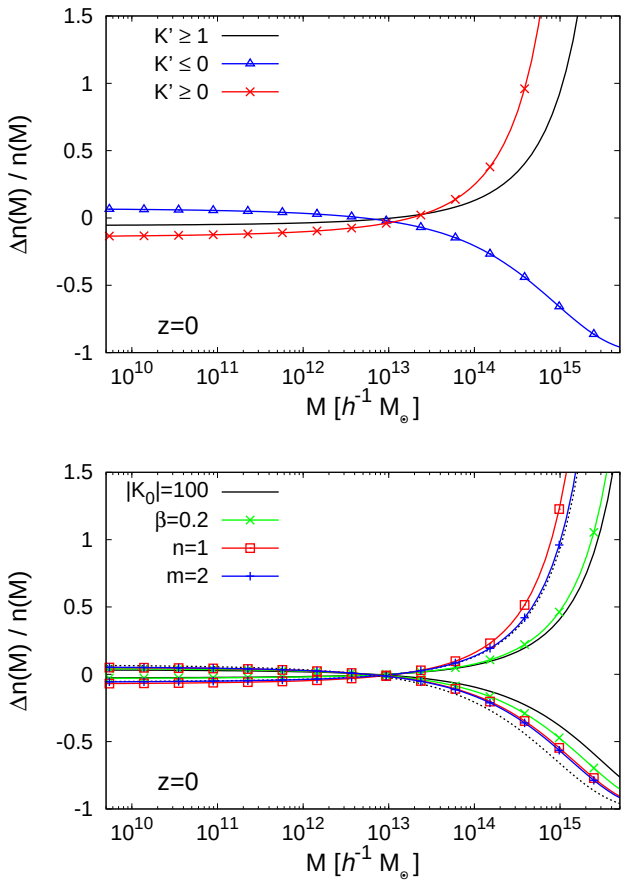


FIG. 8: Relative deviation $[n(M) - n_{\Lambda\mathrm{CDM}}(M)]/n_{\Lambda\mathrm{CDM}}(M)$ of the halo mass function from the Λ-CDM reference, at $z = 0$. *Upper panel:* same models as in the upper panel of Fig. 2. *Lower panel:* same models as in the lower panel of Fig. 2.

Again, the lower panel shows that a higher value of $|K_0|$, or more generally $|\bar{K}'|$, and a smaller β, lead to a smaller deviation from the Λ-CDM reference. The characteristic exponents n and M of the coupling function $A(\varphi)$ and of the kinetic function $K(\chi)$ do not have a great quantitative impact.

C. Halo mass function

As usual, we write the comoving halo mass function $n(M)\mathrm{d}M/M$ as

$$n(M)\frac{\mathrm{d}M}{M} = \frac{\bar{\rho}_0}{M} f(\nu)\frac{\mathrm{d}\nu}{\nu}, \quad \text{with} \quad \nu = \frac{\delta_{L(\Lambda)}}{\sigma_{(\Lambda)}(M)}. \quad (116)$$

Here $\sigma_{(\Lambda)}(M)$ is the root mean square of the linear density contrast at scale M and $\delta_{L(\Lambda)}$ is the linear density contrast associated with the nonlinear density threshold of 200 that defines the virialized halos, both being translated from the initial conditions by the Λ-CDM growth factor $D_{+\Lambda\mathrm{CDM}}(z_0)/D_{+\Lambda\mathrm{CDM}}(z_i)$ as explained in Sec. V B. Thus, the scaling variable ν directly measures the probability of density fluctuations in the Gaussian initial conditions. Then, we take for the scaling function $f(\nu)$ the fit to Λ-CDM simulations obtained in [20], which obeys the exponential tail $f(\nu) \sim e^{-\nu^2/2}$ at large ν. This means that the mass function (116) shows the correct large-mass tail, which is set by the Gaussian initial conditions and the relationship between the current nonlinear density contrast δ and the associated initial linear density contrast δ_{Li} [or equivalently $\delta_{L(\Lambda)}$], which was obtained in Sec. V B. The deviation from the Λ-CDM reference at low mass is not meant to be accurately reproduced by this model (e.g., we neglect any dependence on modified gravity of the exponent of the low-mass power law tail). However, the low-mass range is not very important for our purposes and it is constrained by the normalization condition $\int (M/\overline{\rho}_0) n(M)\mathrm{d}M/M = 1$, which is automatically satisfied by our simple approximation.

We show our results in Fig. 8. As usual, the deviation from the Λ-CDM reference is most important at high mass because the Gaussian cutoff $e^{-\nu^2/2}$ amplifies the sensitivity of rare events to the collapse dynamics. In agreement with the results obtained in the previous sections, models with $K_0 > 0$, or more generally $\bar{K}' > 0$, lead to a faster matter clustering and to a greater number of rare massive halos, while $\bar{K}' < 0$ leads to fewer massive halos. (The normalization constraint to unity implies that the deviation from the Λ-CDM mass function changes sign between the high-mass and low-mass tails.) Again, a higher $|K_0|$ or a lower $|\beta|$ implies smaller deviations from the Λ-CDM reference and the results are mostly sensitive to the parameters K_0 and β.

VI. NONLINEAR MATTER POWER SPECTRUM

Following the method built in [21] for the Λ-CDM scenario, and applied to several modified-gravity models in [9], we combine the one-loop perturbation theory obtained in Sec. III C with a halo model to obtain the nonlinear matter density power spectrum from small to large wave numbers. By construction, this power spectrum agrees with Eq.(94) when it is expanding up to order P_{L0}^2. In the halo model that governs its high-k limit, we take into account the impact of the modified gravity on the nonlinear dynamics through the halo mass function (116) (i.e., through the acceleration or slowing down of the spherical collapse), but we neglect the impact of the modified gravity on the halo profiles (i.e., we keep the NFW profile from [22] and the mass-concentration relation from [21]).

We show our results in Figs. 9 and 10. At low k we recover the one-loop power spectra shown in Fig. 4, with an almost k-independent relative deviation from the Λ-CDM reference, because of the scale independence of our modified-gravity models in the regime (63).

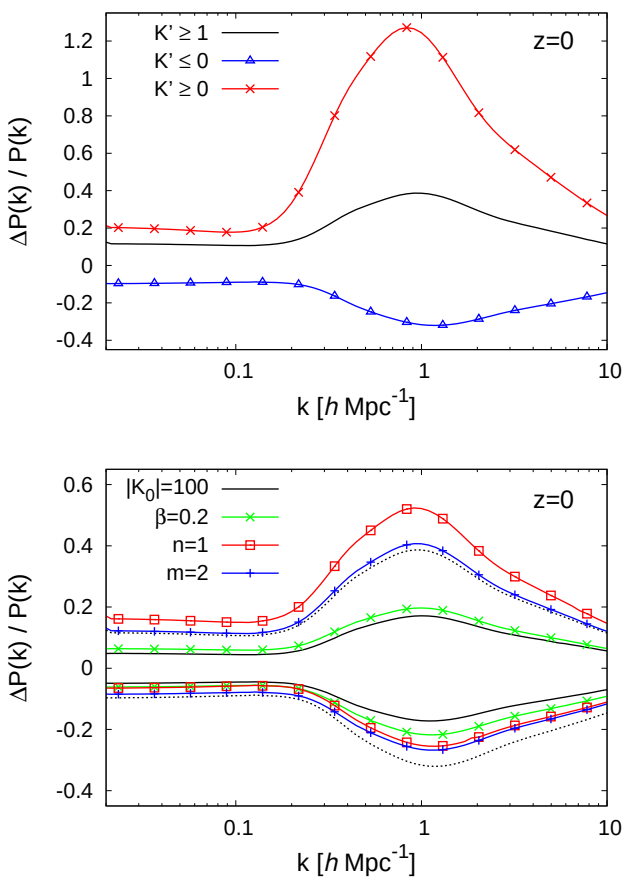


FIG. 9: Relative deviation $[P(k) - P_{\Lambda\rm CDM}(k)]/P_{\Lambda\rm CDM}(k)$ of the nonlinear matter density power spectrum from the Λ-CDM reference, at redshift $z = 0$. *Upper panel:* same models as in the upper panel of Fig. 2. *Lower panel:* same models as in the lower panel of Fig. 2.

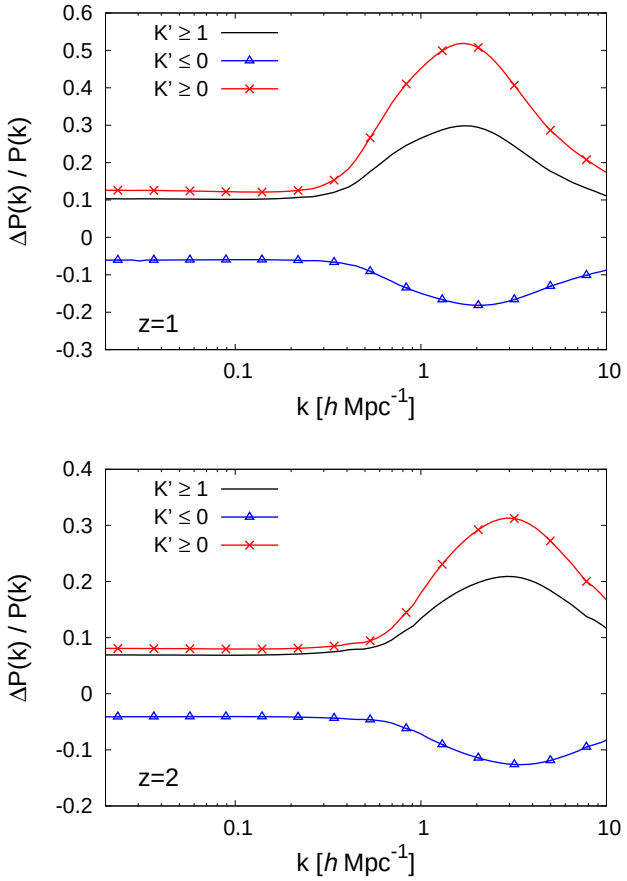


FIG. 10: Same as in the upper panel of Fig. 9, but at redshifts $z = 1$ (upper panel) and $z = 2$ (lower panel).

The deviations are amplified on mildly nonlinear scales, $k \sim 1h\mathrm{Mpc}^{-1}$ at $z = 0$, as they become sensitive to later stages of the nonlinear dynamics and to the large-mass tail of the halo mass function (see for instance [23]). At higher k the relative deviations decrease because the power spectrum is governed by the low-mass tail of the halo mass function and the inner halo density profiles. However, we may underestimate the signal at $k \gtrsim 10h\mathrm{Mpc}^{-1}$ because we neglected the impact of the modification of gravity on these halo profiles.

Again, the sign of the deviation from the Λ-CDM reference depends on the sign of K_0, or $\bar{K}'$, and the results are mostly sensitive to K_0 and β^2.

The deviation from the Λ-CDM prediction decreases at high redshift, because we normalize the linear power spectra to the same initial value at early times, far in the matter era. However, we can see in Fig. 10 that this decrease is rather slow and that significant deviations are already present at $z = 2$ in the matter power spectrum.

The comparison with the background results obtained in the companion paper [6] shows that the relative deviations are significantly greater, by about a factor 10, for $P(k)$ than for background quantities such as the Hubble expansion rate $H(z)$. Therefore, large-scale structures provide a useful probe of such modified-gravity scenarios. In particular, it is possible to keep a background evolution that is very close the the Λ-CDM cosmology, at the percent level, while obtaining significant departures in terms of the matter clustering, at the 10% level [in terms of $P(k)$, higher-order statistics such as the bispectrum, or the high-mass tail of the halo mass function, can show even greater deviations].

VII. COMPARISON WITH OTHER MODELS

In this section, we compare our results with the ones of the chameleon-$f(R)$ models [24, 25], the dilatons [26], the symmetrons [27], the DGP model [28] and the Galileon theories [10, 11] when the N-body simulations are available.

Let us start with the chameleons, dilatons and symmetrons. For all these models, the background follows

the one of Λ-CDM. At the perturbative level, and first in the linear theories, deviations from GR occur on scales lower than the Compton wavelength of the scalar field [29]. As Solar System tests and the screening of the Milky Way imply that the cosmological range of the scalar must be less than 1 Mpc [30], the effects of these models on linear scales are suppressed and only in the quasilinear to mildly nonlinear regimes one can expect to see significant deviations. Symmetrons and dilatons screen gravity in a stronger way in the local environment implying that constraints on these models are less severe than on chameleon-$f(R)$ theories. This implies that the effects of the symmetron and to a lesser extent of the dilaton on large-scale structures are enhanced compared to chameleon-$f(R)$ models. Typically, one expects to see a peak in the deviations from GR on the scales corresponding to the range of the scalar field, especially in the power spectrum of density fluctuations [9]. On small and large scales, the models converge towards GR. On small scales, this is due to the screening effect and on large scales this is also the screening property outside the Compton radius.

For the DGP model on the self-accelerated branch [28], the background is modified compared to Λ-CDM with an increase of H compared to Λ-CDM. At the perturbative level, the DGP model leads to a scale-independent decrease of Newton's constant on large and linear scales. On nonlinear scales, the Vainshtein mechanism reduces the negative deviations from GR and applies on scale as large as $0.1h\mathrm{Mpc}^{-1}$. Moreover, the overall deviation from GR is significantly reduced, even on large scales, at redshifts $z = 1$ and $z = 2$. This comes from the fact that the deviation of the background from Λ-CDM is a late-time effect.

The cubic and quartic Galileon models [10, 11] have been simulated with differences between the two models. In both cases, the background evolution follows a tracker solution where $\dot{\varphi}$ goes like $1/H$, i.e. the field varies more with time in the recent past implying a stronger effect on the growth of structure on large scales in the linear regime. In both the cubic and quartic scales, the effective Newton constant is larger than in GR in sparse regions of the Universe. The Vainshtein mechanism operates on very mildly quasilinear scales as soon as $0.03h\mathrm{Mpc}^{-1}$ where nonlinear effects cannot be neglected. Moreover, in the densest regions the effective Newton constant changes sign in the quartic case and becomes smaller than in GR. As in the DGP case, the deviations from GR decrease significantly from $z = 0$ to $z = 1$ and beyond $z = 1$ the nonlinear effects of the Galileon models can be neglected and the models behave like linear theories with a time dependent but scale-independent Newton constant.

The K-mouflage models also have a modified background evolution which becomes prominent in the recent past of the Universe and deviations from Λ-CDM are significant from a redshift $z \sim 5$ with maximal extension between $z = 1$ and $z = 2$. At the perturbative level, linear effects depend on a time dependent Newton constant and a new friction term implying that the growing mode and the growth rate are enhanced for $K_0 > 0$ and depleted when $K_0 < 0$ compared to Λ-CDM. As the K-mouflage models do not screen the quasilinear structures of the Universe, we find that linear features persist beyond the linear regime. We find that the one loop contribution to perturbation theory is negligible and that, in fact, the K-mouflage models behave like a linear model in the scalar sector. Nonlinearities are only present as usual in the matter sector. These nonlinearities imply that the deviation from Λ-CDM of the power spectrum have a peak at the onset of the nonlinear regime around $1\ h\mathrm{Mpc}^{-1}$ for $z = 0$. In the nonlinear regime, the critical linear density contrast is smaller than the Λ-CDM one for $K_0 > 0$ in a scale-independent way, leading to an increase in the number of large-mass clusters for $K_0 > 0$. We have also studied the evolution of the deviations from Λ-CDM with the redshift and shown that they increase in the recent past corresponding to the maximal deviations of the background from Λ-CDM between $z = 1$ and $z = 2$. Moreover, when subtracting the power spectrum calculated with the modified background (QCDM, see App. B), we find that the influence of the new friction term and the modified Newton constant on linear scales and their extension to the nonlinear regime are not negligible and vary very little from $z = 0$ to $z = 2$, apart from a shift in the peak of the power spectrum due to the change of the onset of nonlinearities with the redshift.

Hence we can draw general conclusions about the differences between the three types of screening mechanisms at the cosmological level. Models with the Vainshtein and K-mouflage properties have a modified background cosmology when chameleonlike models follow Λ-CDM. The deviations from Λ-CDM are more pronounced for K-mouflage models at redshifts of a few than for Vainshtein-like models. Structures grow differently too. On linear scales, chameleons converge to GR while models of the K-mouflage and Vainshtein types show deviations there. K-mouflage models do not screen quasilinear structures whereas chameleonlike and Vainshtein models do. Moreover, K-mouflage models have deviations from Λ-CDM which persist up to redshifts of a few when for the other types of screening the effects become less significant. These features are sufficiently different to hope to distinguish these models if modified gravity effects were to be detected by future surveys.

VIII. SUMMARY AND CONCLUSION

A. Summary

Before we conclude this paper, let us briefly summarize the main properties of the K-mouflage models studied here and our results:

- K-mouflage models involve an additional scalar field, φ, with a nonstandard nonlinear kinetic term, $\mathcal{M}^4 K[-(\partial\varphi)^2/2\mathcal{M}^4]$, where $\mathcal{M}^4$ is of the order of the

critical density now. Here we consider models where the field φ is also conformally coupled to matter fields through the Jordan metric $\tilde{g}_{\mu\nu} = A^2(\varphi) g_{\mu\nu}$.

- The nonlinearity of the Lagrangian, which gives rise to terms $\bar{K}'(\partial\delta\varphi)^2$ for the fluctuations with respect to the cosmological background, provides a "screening mechanism" as the large prefactor $\bar{K}'$ freezes the fluctuations and suppresses the fifth force in the high-density and small-scale regimes. This provides a convergence to GR on small astrophysical scales (studied in an upcoming paper) and at high redshift [6]. On the other hand, in contrast with some other modified-gravity scenarios (e.g., chameleon and Galileon models), linear cosmological structures are unscreened and show deviations from Λ-CDM up to the Hubble scale. Moreover, the dark energy background evolution of K-mouflage models only behaves as a cosmological constant at low redshifts.

- The equations of motion obtained for matter on cosmological scales are the usual continuity equation, a modified Euler equation (with an additional friction term and an additional fifth-force potential term), and a modified Poisson equation (with a time dependent effective Newton constant). The scalar field fluctuations obey a time dependent Klein-Gordon equation, as the background field evolves with time.

- Even though this background does not follow a quasistatic evolution, on small scales (far below the horizon) the scalar field fluctuations obey a quasistatic regime (because spatial gradients dominate over time derivatives) and are "slaved" to the same-time density fluctuations (i.e., the Klein-Gordon equation takes the form of a nonlinear Poisson equation).

- For cosmological structures, from the cosmic web down to clusters of galaxies, which show moderate density contrasts ($\delta \lesssim 200$), this quasistatic Klein-Gordon equation can be linearized. Therefore, these models provide an explicit nonlinear example where the scalar field sector can be linearized on cosmological scales (while the nonlinearity appears on smaller astrophysical scale and ensures the convergence back to GR).

- Quasilinear scales can be studied using cosmological perturbation theory as in the standard Λ-CDM scenario, taking into account the new linear friction and fifth-force terms in the Euler equation. In particular, the nonlinearities are due to the usual transport terms that are identical to those found in the Λ-CDM case.

- The linear regime growth factors differ from the Λ-CDM predictions through time dependent terms, but in contrast with some other modified-gravity models, they do not show an additional scale dependence (because large scales remain unscreened up to the horizon). The sign of the deviation from Λ-CDM is set by the sign of the derivative $\bar{K}'$, as for background quantities [6]. For instance, models with $K' > 0$ yield a smaller Hubble expansion rate $H(z)$ (with a common normalization today) and larger linear growth rates $D_+(z)$ and $f(z)$. More precisely, the quantity that governs the deviations from the Λ-CDM predictions, both for the background and the perturbations, is the ratio $\beta^2/\bar{K}'$, where β is the coupling constant to the matter. As for small-scale screening, these deviations are suppressed in models with a large nonlinear factor $\bar{K}'$.

- Because large linear scales deviate from the Λ-CDM predictions, large-scale CMB anisotropies also show a significant deviation through the ISW effect. In particular, the cross-correlation between the large-scale CMB temperature fluctuations and low-redshift galaxy surveys can change sign for models with $K' < 0$, and the amplitude of the relative deviation from Λ-CDM grows with redshift. This also gives rise to a deviation for the low-ℓ CMB multipoles C_ℓ, but this generically yields more power than the Λ-CDM prediction over $\ell \leq 10$ whatever the sign of $\bar{K}'$.

- To go beyond the perturbative regime, we have also studied the spherical collapse dynamics. For the same reason as the absence of scale dependence in the linear regime, the spherical collapse is only modified by time dependent but scale-independent factors. This also means that, as in GR or Newtonian gravity, different mass shells remain uncoupled until shell crossing. This simplifies the analysis and it leads to a time dependent linear density contrast threshold $\delta_L(z)$ for the collapse of virialized halos. This yields in turn a deviation for the large-mass tail of the halo mass function, that again depends on the sign of $\bar{K}'$.

- Combining perturbation theory and the spherical collapse dynamics, we have estimated the matter power spectrum up to mildly nonlinear scales $k \lesssim 10h\mathrm{Mpc}^{-1}$. We recover a constant relative deviation from Λ-CDM on linear scales and a peak on weakly nonlinear scales, $k \sim 1h\mathrm{Mpc}^{-1}$, due to the amplification associated with the nonlinear matter dynamics and the large-mass tail of the halo mass function. Therefore, large-scale structures provide a useful probe of such models as the deviations from Λ-CDM for $P(k)$, or the halo mass function, can be greater by a factor of 10 than those of background quantities, such as $H(z)$.

- These deviations decrease rather slowly at higher redshift and remain non-negligible at $z = 2$ (as compared to $z = 0$). This is due to the fact that the dark energy component only slowly becomes subdominant at high z, because its energy density actually grows (but at a smaller rate than the matter density). This feature is rather different from the behavior obtained in some other modified-gravity models [e.g., $f(R)$ theories or dilaton models] where the background is almost identical to Λ-CDM and the deviations for matter perturbations are only significant at low z.

B. Conclusions

In conclusion, K-mouflage is an alternative to the screening by the chameleon or the Vainshtein mechanisms with striking features on the growth of large-scale structures. The most significant one is certainly the ab-

sence of screening of large astrophysical objects on cosmological scales, such as galaxy clusters. In this regime, the scalar theory behaves like a linear field theory leading to a time dependent modification of Newton's constant and an increase/decrease of the growth of structure compared to Λ-CDM depending on the ratio $\beta^2/\bar{K}'$ corresponding to the square of the effective coupling to matter when the bare coupling β is rescaled by the wave function normalization of the field $|\bar{K}'|^{1/2}$. For models where deviations from the Λ-CDM behavior at the background level are at the percent level, the deviations of the power spectrum of the density contrast on mildly nonlinear scales is enhanced compared to the linear part of the spectrum and can reach ten percent. Moreover, the convergence to the Einstein- de Sitter behavior of perturbations in the past is rather slow due to the properties of the background cosmology. Indeed, at the background level, the Hubble rate converges to the Einstein- de Sitter case in the distant past due to the screening of the scalar field in the high-density environment of the early Universe while it converges to a Λ-CDM behavior in the very recent past. In the intermediate regime around redshifts of $1 \lesssim z \lesssim 2$, the Hubble rate can differ significantly from its Λ-CDM counterpart. This translates into a relative persistence of the deviations from Λ-CDM which differs from other screening mechanisms, up to redshifts of a few. We leave a more detailed analysis of cosmological observational constraints to future works. K-mouflage could also have different features on smaller scales where the density contrast is larger than in galaxy clusters. In this regime, the nonlinearities of the models reappear and cannot be neglected, especially on scales of the order of the K-mouflage radius. This is left for future work.

Acknowledgments

This work is supported in part by the French Agence Nationale de la Recherche under Grant ANR-12-BS05-0002. Ph. B. acknowledges partial support from the European Union FP7 ITN INVISIBLES (Marie Curie Actions, PITN- GA-2011- 289442) and from the Agence Nationale de la Recherche under contract ANR 2010 BLANC 0413 01.

Appendix A: Perturbations

In this appendix we derive the perturbation equations used in the text. First of all, the energy-momentum tensor of a CDM fluid is

$$T^{\mu\nu} = \rho_E u^\mu u^\nu \tag{A1}$$

where ρ_E is the energy density in the Einstein frame and u^μ is the velocity 4-vector normalized such that $u^\mu u_\mu = -1$, where indices are raised or lowered using the Einstein metric $g_{\mu\nu}$. Notice that we have the identification $u^\mu = \frac{\mathrm{d}x^\mu}{\mathrm{d}\mathcal{T}}$ where $\mathcal{T}$ is the proper time and $\mathrm{d}\mathcal{T}^2 = -g_{\mu\nu}\mathrm{d}x^\mu\mathrm{d}x^\nu$. In terms of perturbations in the conformal Newton gauge, where

$$\mathrm{d}s^2 = a^2[-(1+2\Psi_\mathrm{N})\mathrm{d}\tau^2 + (1-2\Psi_\mathrm{N})\mathrm{d}\mathbf{x}^2], \tag{A2}$$

we have $u^\mu = a^{-1}(1-\Psi_\mathrm{N}+v_jv^j/2, v^i)$ where v^i is the velocity vector of CDM particles identified to leading order as $v^i = \frac{\mathrm{d}x^i}{\mathrm{d}\tau}$ and we also have to leading order $\mathrm{d}\mathcal{T} = a\mathrm{d}\tau\sqrt{1+\Psi_\mathrm{N}-v^iv_i/2}$. Here and throughout this paper, the particles are nonrelativistic and Newton's potential is small, and we only keep terms up to first order over Ψ_N and v^2 (within virialized halos we have $v^2 \sim \Psi_\mathrm{N}$). The Bianchi identity and the Klein-Gordon equations imply that matter is not conserved but

$$D_\mu T^{\mu\nu}_{(\mathrm{m})} = -\rho_E\,\partial^\nu(\ln A). \tag{A3}$$

This follows directly from $G^{\mu\nu} = 8\pi\mathcal{G}[T^{\mu\nu}_{(\mathrm{m})} + T^{\mu\nu}_{(\varphi)}]$ and $D_\mu G^{\mu\nu} = 0$, leading to $D_\mu T^{\mu\nu}_{(\mathrm{m})} = -D_\mu T^{\mu\nu}_{(\varphi)}$ where $T^{\mu\nu}_{(\varphi)} = K'\partial^\mu\varphi\partial^\nu\varphi + g^{\mu\nu}\mathcal{M}^4K$. The Klein-Gordon equation is

$$D_\mu(\partial^\mu\varphi K') = -\beta\frac{T}{M_\mathrm{Pl}}, \tag{A4}$$

where

$$\beta = M_\mathrm{Pl}\frac{\mathrm{d}\ln A}{\mathrm{d}\varphi}. \tag{A5}$$

Using this we easily get (A3) with $T = -\rho_E$. This gives explicitly

$$\dot\rho_E u^\nu + 3h\rho_E u^\nu + \rho_E u^\mu D_\mu u^\nu = -\rho_E\,\partial^\nu(\ln A) \tag{A6}$$

where we have introduced $\dot\rho_E = u^\mu D_\mu\rho_E$ and the local Hubble rate $3h = D_\mu u^\mu$.

Contracting with u_ν and using $u^2 = -1$, we get

$$\dot\rho_E + 3h\rho_E = \frac{\dot A}{A}\rho_E. \tag{A7}$$

It is easy to see that in perturbations $\dot\rho_E = a^{-1}\left(\rho_E' + v^i\partial_i\rho_E\right)$, whereas $3h = 3H + \frac{\theta}{a}$, where $' = \partial/\partial\tau$ and $H = a'/a^2$, and we have defined $\theta = \partial_i v^i$. Here and in the following, we neglect terms of order Ψ_N or v^2 as compared with unity, as well as their time derivatives Ψ_N' or v^jv_j', and we only keep the first-order spatial gradients such as $\partial^i\Psi_\mathrm{N}$ or $v^j\partial_jv^i$ (because we consider large-scale structures that evolve on the Hubble time scale but are much smaller than the horizon). Therefore this is explicitly

$$\rho_E' + v^i\partial_i\rho_E + (3\mathcal{H}+\theta)\rho_E = (\ln A)'\rho_E + v^i\partial_i(\ln A)\rho_E, \tag{A8}$$

using $\mathcal{H} = a'/a$. Let us use (A7), and defining

$$\rho_E = A\rho, \tag{A9}$$

we get

$$\dot\rho + 3h\rho = 0, \tag{A10}$$

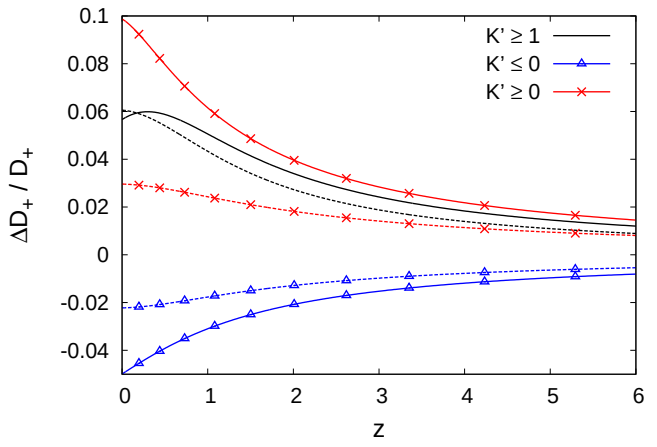


FIG. 11: Relative deviation $[D_+(z) - D_{+\Lambda\mathrm{CDM}}(z)]/D_{+\Lambda\mathrm{CDM}}(z)$ of the linear growing mode from the $\Lambda-$CDM reference. Solid lines: same models as in the upper panel of Fig. 2. Dashed lines: same models but without the factors ϵ_i in Eq.(80).

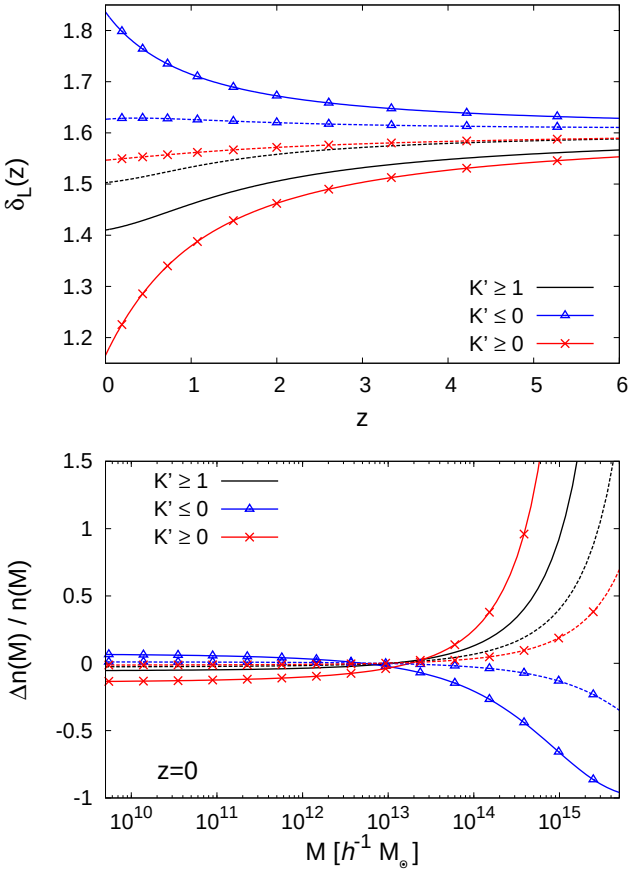


FIG. 12: *Upper panel:* linear density contrast threshold $\delta_{L(\Lambda)}(z)$, for the same models as in the upper panel of Fig. 7, taking into account the factors ϵ_i in Eq.(115) (solid lines) or setting them to zero (dashed lines). *Lower panel:* relative deviation $[n(M) - n_{\Lambda\mathrm{CDM}}(M)]/n_{\Lambda\mathrm{CDM}}(M)$ of the halo mass function from the Λ-CDM reference, for the same cases.

which is nothing but the usual conservation equation for ρ. This can be done also explicitly in (A8) which becomes after a few trivial steps

$$\rho' + \partial_i(\rho v^i) + 3\mathcal{H}\rho = 0, \tag{A11}$$

as one expects.

The nonconservation equation (A6) can now be drastically simplified and leads to

$$u^\nu D_\nu u^\mu = -\frac{\dot{A}}{A}u^\mu - \partial^\mu(\ln A). \tag{A12}$$

This is the generalized geodesic equation. Specializing to $\mu = i$, we get

$$\partial_\tau v^i + \mathcal{H}v^i + v^j\partial_j v^i = -\left(\frac{A'}{A} + v^j\partial_j \ln A\right)v^i - \partial^i(\Psi_\mathrm{N} + \ln A) \tag{A13}$$

as expected for Newton's law and its relativistic corrections. Notice that there is a term in $v^i v^j \partial_j \ln A$ which is small or of order $v^2 \ll 1$ in the nonrelativistic limit compared to $\partial^i \ln A$, and can be safely dropped.

Appendix B: Modified background and dynamics

1. Effect of the factors ϵ_1 and ϵ_2

The linear growing modes $D_+(\eta)$ obtained from Eq.(80) deviate from the Λ-CDM reference because of two effects: (a) the background evolution is different from Λ-CDM (the factors $w_\varphi^{\mathrm{eff}}\Omega_\varphi^{\mathrm{eff}}$ and Ω_m show a different redshift dependence), and (b) there are two new terms ϵ_1 and ϵ_2 in the evolution equation, due to the coupling between the matter density and velocity fluctuations and the scalar field φ.

To disentangle these two effects, we compare in Fig. 11 the results we obtain from the full Eq.(80)), also shown in Fig. 2, with those we obtain when we set the factors ϵ_1 and ϵ_2 to zero in Eq.(80)) (while keeping the modified-gravity background). We can see that a significant part of the deviation from the Λ-CDM reference is merely due to the change of background evolution, especially at $z \geq 1$. However, the importance of the factors ϵ_i depends somewhat on the values of the parameters of the model and they cannot be discarded. In particular, for the model (15) the effect of the factors ϵ_i is quite large.

In a similar fashion, the nonlinear spherical dynamics involve both the modified background factors $w_\varphi^{\mathrm{eff}}\Omega_\varphi^{\mathrm{eff}}$ and Ω_m, and the new terms ϵ_1 and ϵ_2, see Eq.(115). We compare in Fig. 12 the linear density threshold $\delta_{L(\Lambda)}$ and the halo mass function $n(M)$ obtained when we include the factors ϵ_i or not. The deviation from the Λ-CDM

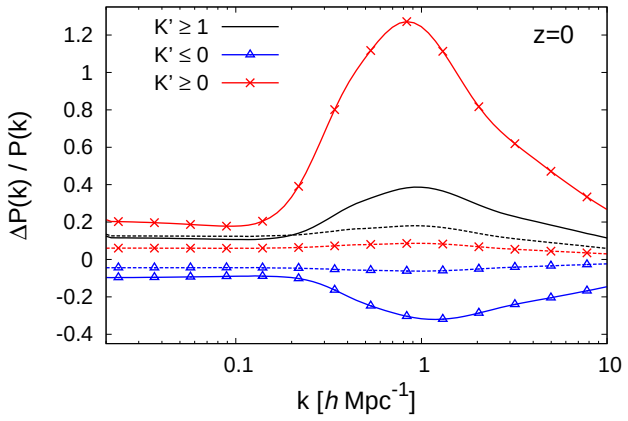


FIG. 13: Relative deviation $[P(k) - P_{\Lambda\mathrm{CDM}}(k)]/P_{\Lambda\mathrm{CDM}}(k)$ of the nonlinear matter density power spectrum from the Λ-CDM reference, at redshift $z = 0$, for the same models as in Fig. 9, where we keep the factors ϵ_i (solid lines) or set them to zero (dashed lines).

reference keeps the same sign whether we include these factors or not, as for the linear modes shown in Fig. 11, but the quantitative impact of the factors ϵ_i is greater and they cannot be neglected.

We also compare the matter density power spectra obtained by keeping the factors ϵ_i or setting them to zero in Fig. 13. The difference between these cases agrees with the results found in Figs. 11 and 12. Neglecting the factors ϵ_i would significantly distort the shape of the deviation from the Λ-CDM power spectrum and underestimate this deviation, especially on mildly nonlinear scales.

2. Comparison with the QCDM reference

Finally, we have studied the effect of the parameters $\epsilon_{1,2}$ by subtracting the power spectrum and halo mass function calculated with the modified background (QCDM). In agreement with the results above, the deviations from GR are not entirely due to the modified background and one can clearly see in Figs. 14 and 15 that the modified perturbation dynamics play a significant role. The order of magnitude of the deviation does not change much from $z = 0$ to $z = 2$, a key feature of the K-mouflage models, except for the model (15) where there is a strong evolution at $z \lesssim 2$ and a slower evolution at higher redshifts than for models (13) and (14).

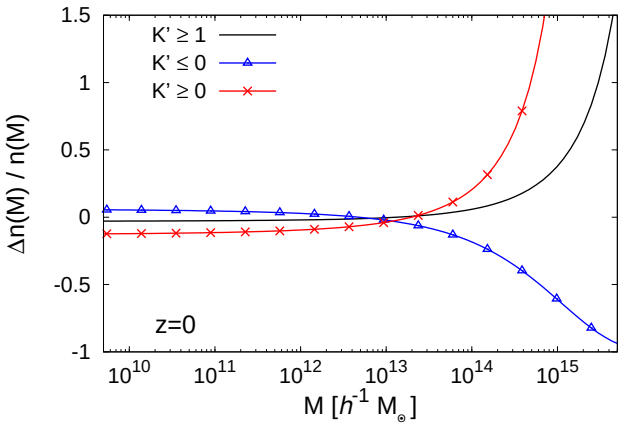


FIG. 14: Relative deviation $[n(M) - n_{\mathrm{QCDM}}(M)]/n_{\mathrm{QCDM}}(M)$ of the halo mass function from the QCDM reference, for the same cases as in the upper panel of Fig. 8.

[1] E. J. Copeland, M. Sami, and S. Tsujikawa, Int.J.Mod.Phys. **D15**, 1753 (2006), hep-th/0603057.
[2] J. Khoury (2010), 1011.5909.
[3] C. Will, Pramana **63**, 731 (2004).
[4] E. Babichev, C. Deffayet, and R. Ziour, Int.J.Mod.Phys. **D18**, 2147 (2009), 0905.2943.
[5] P. Brax, C. Burrage, and A.-C. Davis, JCAP **1301**, 020 (2013), 1209.1293.
[6] P. Brax and P. Valageas, ArXiv e-prints (2014), 1403.5420.
[7] J. Khoury (2013), 1312.2006.
[8] L. Amendola et al. (Euclid Theory Working Group), Living Rev.Rel. **16**, 6 (2013), 1206.1225.
[9] P. Brax and P. Valageas, Phys. Rev. D **88**, 023527 (2013), 1305.5647.
[10] A. Barreira, B. Li, W. A. Hellwing, C. M. Baugh, and S. Pascoli (2013), 1306.3219.
[11] B. Li, A. Barreira, C. M. Baugh, W. A. Hellwing, K. Koyama, et al., JCAP **1311**, 012 (2013), 1308.3491.
[12] P. Brax and P. Valageas, Phys. Rev. D **86**, 063512 (2012), 1205.6583.
[13] Planck Collaboration, P. A. R. Ade, N. Aghanim, C. Armitage-Caplan, M. Arnaud, M. Ashdown, F. Atrio-Barandela, J. Aumont, C. Baccigalupi, A. J. Banday, et al., ArXiv e-prints (2013), 1303.5076.
[14] R. K. Sachs and A. M. Wolfe, Astrophys. J. **147**, 73 (1967).
[15] A. Cooray, Phys. Rev. D **65**, 103510 (2002), astro-ph/0112408.
[16] N. Afshordi, Phys. Rev. D **70**, 083536 (2004), arXiv:astro-ph/0401166.
[17] B. R. Granett, M. C. Neyrinck, and I. Szapudi, Astrophys. J. **701**, 414 (2009), 0812.1025.
[18] R. Mainini and D. F. Mota, Astrophys. J. **744**, 3 (2012), 1011.0083.
[19] G. Hinshaw, D. Larson, E. Komatsu, D. N. Spergel, C. L. Bennett, J. Dunkley, M. R. Nolta, M. Halpern, R. S. Hill, N. Odegard, et al., *Astrophys. J. Suppl. Ser.* **208**,

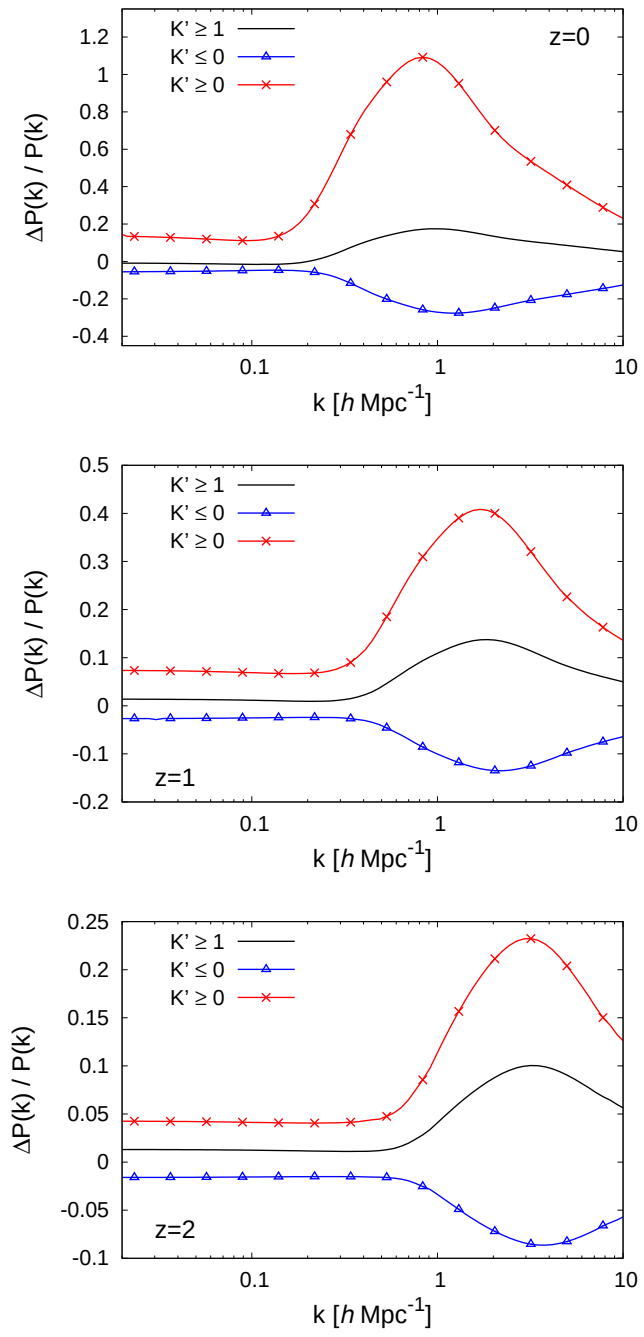


FIG. 15: Relative deviation $[P(k) - P_{\rm QCDM}(k)]/P_{\rm QCDM}(k)$ of the nonlinear matter density power spectrum from the QCDM reference, at redshifts $z = 0, 1$, and 2, for the same models as in the upper panel of Fig. 9.

19 (2013), 1212.5226.
[20] P. Valageas, *Astr. & Astrophys.* **508**, 93 (2009), 0905.2277.
[21] P. Valageas, T. Nishimichi, and A. Taruya, ArXiv e-prints (2013), 1302.4533.
[22] J. F. Navarro, C. S. Frenk, and S. D. M. White, Astrophys. J. **490**, 493 (1997), arXiv:astro-ph/9611107.
[23] P. Valageas, Phys. Rev. D **88**, 083524 (2013), 1308.6755.
[24] P. Brax, A.-C. Davis, B. Li, H. A. Winther, and G.-B. Zhao (2013), 1303.0007.
[25] B. Li, W. A. Hellwing, K. Koyama, G.-B. Zhao, E. Jennings, et al. (2012), 1206.4317.
[26] P. Brax, C. van de Bruck, A.-C. Davis, B. Li, and D. J. Shaw, Phys.Rev. **D83**, 104026 (2011), 1102.3692.
[27] P. Brax, A.-C. Davis, B. Li, H. A. Winther, and G.-B. Zhao, JCAP **1210**, 002 (2012), 1206.3568.
[28] B. Li, G.-B. Zhao, and K. Koyama, JCAP **1305**, 023 (2013), 1303.0008.
[29] P. Brax, C. van de Bruck, A. Davis, J. Khoury, and A. Weltman, AIP Conf.Proc. **736**, 105 (2005), astro-ph/0410103.
[30] P. Brax, A.-C. Davis, and B. Li (2011), 1111.6613.
[31] As for the usual Newtonian gravity, this means that if the initial conditions had very little power on large scales (i.e., the linear power spectrum $P_L(k)$ would decay faster than k^4 at low k), nonlinearities would only generate a k^4 tail at low k.